Volume 6 Number 4 Oct - Dec 2017

STUDENT JOURNAL OF PHYSICS

INTERNATIONAL EDITION

INDIAN ASSOCIATION OF PHYSICS TEACHERS

ISSN – 2319-3166

STUDENT JOURNAL OF PHYSICS

This is a quarterly journal published by Indian Association Of Physics Teachers. It publishes research articles contributed by Under Graduate and Post Graduate students of colleges, universities and similar teaching institutions, as principal authors.

Registered Office

Editor-in-Chief, SJP, Institute of Physics, Sainik School, Bhubaneswar, Odisha, India – 751005
(www.iopb.res.in/~sjp/)

STUDENT JOURNAL OF PHYSICS

Scope of the Journal

The journal is devoted to research carried out by students at undergraduate level. It provides a platform for the young students to explore their creativity, originality, and independence in terms of research articles which may be written in collaboration with senior scientist(s), but with a very significant contribution from the student. The articles will be judged for suitability of publication in the following two broad categories:

1. **Project based articles**
   These articles are based on research projects assigned and guided by senior scientist(s) and carried out predominantly or entirely by the student.
2. **Articles based on original ideas of student**
   These articles are originated by the student and developed by him/ her with possible help from senior advisor. Very often an undergraduate student producing original idea is unable to find a venue for its expression where it can get due attention. SJP, with its primary goal of encouraging original research at the undergraduate level provides a platform for bringing out such research works.
   It is an online journal with no cost to the author.

Since SJP is concerned with undergraduate physics education, it will occasionally also publish articles on science education written by senior physicists.

Information for Authors

- Check the accuracy of your references.
- Include the complete source information for any references cited in the abstract. (Do not cite reference numbers in the abstract.)
- Number references in text consecutively, starting with [1].

- Language: Papers should have a clear presentation written in good English. Use a spell checker.

Submission

1. Use the link "Submit" of Website to submit all files (manuscript and figures) together in the submission (either as a single .tar file or as multiple files)
2. Choose one of the Editors in the link "Submit" of Website as communicating editor while submitting your manuscript.

Preparation for Submission

Use the template available at "Submit" section of Website for preparation of the manuscript.

Re-Submission

- For re-submission, please respond to the major points of the criticism raised by the referees.
- If your paper is accepted, please check the proofs carefully.

Scope

- SJP covers all areas of applied, fundamental, and interdisciplinary physics research.

STUDENT JOURNAL OF PHYSICS

Determination of cross section for top quark pair production at LHC and study of jets from top quark decays

Sarvesh Bansal[1]*and **Kajari Mazumdar**[2]
[1]M.Sc Physics 2nd year, Physics Department, IIT Delhi
[2]Department of High Energy Physics, TIFR, Mumbai

Abstract. Currently high energy physicists are trying to find particles beyond the standard model. These new energetic particles will have top quark as their major background. So to understand these new particles we need to understand the kinematics of top quark in a better way. In this project we have estimated the production cross section of top quark pair in LHC proton-proton collision at centre of mass energy of 7 TeV using processed data made available in open platform by CMS collaboration at LHC, CERN. Also in this project we have studied the situation of boosted top quarks when LHC machine will collide protons at an energy of 14 TeV. We have studied the jets from these boosted top quark by generating samples using Pythia Monte Carlo event generator .We used N-subjettiness parameter to find some characteristics of these jets in order to distinguish top signal from mainly QCD multijets events.

Keywords: Top Quark Decay, CMS Collaboration, LHC.

1. INTRODUCTION

In the first part of this project we have estimated the production cross section of top quark [1-4] pair in LHC proton-proton collision at centre-of-mass energy of 7 TeV using processed data made available in open platform by CMS collaboration at LHC, CERN.
(http://opendata.cern.ch/collection/CMS-Derived-Datasets).

This data corresponds to an integrated luminosity of 50 pb^{-1} and each event has at least one muon in the final state as reconstructed by the CMS detector. When a top quark decays (t $\rightarrow$bW) it gives 1 or 3 jets depending on semil-leptonic or fully hadronic mode. Thus top quark pair events in the data sample must additionally have jets, with at least two jets due to b-quarks (from top and anti-top) and missing transverse energy due to neutrino. Using Monte Carlo event samples for signal and various background processes we have studied the kinematics of final state objects and applied various selection criteria to enhance the signal-to-background ratio of the final sample. The purity of the selected sample and the efficiency of selection are estimated from Monte Carlo. The cross section is estimated using experimental data.

*bansalsarvesh.s@gmail.com

In the second part of the project we have studied the situation of boosted top quarks when LHC machine will collide protons at an energy of 14 TeV. At lower energy collisions the jets from a top quark hadronic decay are distinguishable since they are separated. But at high energy collisions when the top quark is itself boosted, jets from a top decay are not separable always within the detector and may be detected as a fat jet. We have studied these boosted top quark jets by generating samples using Pythia Monte Carlo event generator and used Fastjet method for jet reconstruction. We looked into the jet substructures using N-subjettiness to find some characteristics of these jets in order to distinguish top signal from mainly QCD multijets events.

2. PRODUCTION AND DECAY OF TOP QUARK

Top quark can be produced in high energy colliders by two processes.

- Electroweak interaction
- Strong interaction

In electroweak interaction only single top quark is produced with other particles and jets, but in strong interaction top quarks are produced in pair and with significantly large rate. Top quark is a heavy and unstable particle so it decays very fast. It decays mostly(branching ratio 99 %)by single mode.

$$\mathrm{t} \rightarrow \mathrm{W}^{+}\mathrm{b}$$

Now W can decay into leptons $\mathrm{W} \rightarrow \ell\nu$ where $\ell = e, \mu, \tau$ or hadrons $\mathrm{W} \rightarrow \mathrm{q}_1\bar{\mathrm{q}}_2$ where $\mathrm{q}_1, \mathrm{q}_2 = \mathrm{u}, \mathrm{d}, \mathrm{c}, \mathrm{s}, \mathrm{b}$. Thus we can have three types of final states when a $\mathrm{t}\bar{\mathrm{t}}$ is produced.Figure 1 displays the cartoons of these (Br is an abbreviation used for branching ratio.).

- Semi-leptonic; $\mathrm{t} \rightarrow \mathrm{b}\ell^{+}\nu$ and $\bar{\mathrm{t}} \rightarrow \bar{\mathrm{b}}\mathrm{q}_1\bar{\mathrm{q}}_2$ and visa versa (Br $\approx$ 36%)
- Fully Hadronic; $\mathrm{t} \rightarrow \mathrm{b}\mathrm{q}_1\bar{\mathrm{q}}_2$ and $\bar{\mathrm{t}} \rightarrow \bar{\mathrm{b}}\mathrm{q}_3\bar{\mathrm{q}}_4$ (Br $\approx$ 45%)
- Dileptonic; $\mathrm{t} \rightarrow \mathrm{b}\ell^{+}\nu$ and $\bar{\mathrm{t}} \rightarrow \bar{\mathrm{b}}\ell^{-}\bar{\nu}$ (Br $\approx$ 7%)

We have done the analysis of semi-leptonic decay. In semi leptonic decay of $t\bar{t}$ event, final state involves a charged lepton, a corresponding neutrino and at least four jets out of which there are two b-tag jets. Semi-leptonic decay can be divided into three modes with three different leptons μ, e, τ.

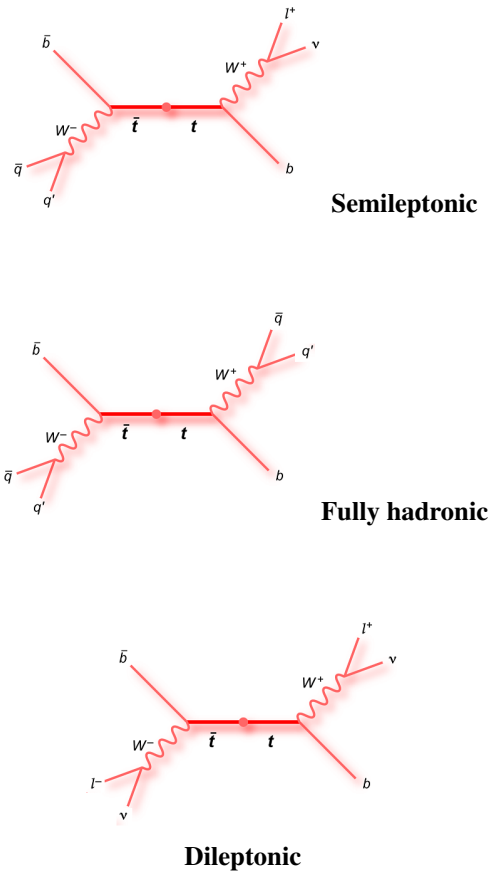

Figure 1. Figure shows the final states of top quark pair. Top quark decays via $\mathrm{t} \rightarrow \mathrm{W}^{+}\mathrm{b}$. Further W can decay into leptons $\mathrm{W} \rightarrow \ell\nu$ where $\ell = e, \mu, \tau$ or hadrons $\mathrm{W} \rightarrow \mathrm{q}_1\bar{\mathrm{q}}_2$ where $\mathrm{q}_1, \mathrm{q}_2 = \mathrm{u}, \mathrm{d}, \mathrm{c}, \mathrm{s}, \mathrm{b}$. Antitop quark also decays similarly. So t and $\bar{\mathrm{t}}$ collectively gives three final states a) Semileptonic b) Fully Hadronic c) dileptonic. Details are given in the figure above.

3. ESTIMATION OF CROSS SECTION

3.1 *Background*

There are many other processes which give the same final state as that of $\mathrm{t}\bar{\mathrm{t}}$ event with semileptonic final state. These are considered as backgrounds. These processes are

- **W + jets, Z + jets** : W/Z + jets are produces in hadron-hadron collisions. A quark from one hadron and anti-quark from another hadron get annihilated and produce W/Z. Before annihilation these quarks emit gluons which on hadronisation give us jets.

- **Di-boson**

  1. **WW**: These are produced in following way.
     a) $q\bar{q} \rightarrow Z \rightarrow W^+W^-$ and b) $gg \rightarrow Z \rightarrow W^+W^-$.
  2. **ZZ**: these are also produced in similar way to WW just by replacing WW by ZZ in the final state.
     a) $q\bar{q} \rightarrow Z \rightarrow ZZ$ and b) $gg \rightarrow Z \rightarrow ZZ$.
  3. **WZ**: This can be produced by interaction of quark and antiquark of different kinds which produce a W and W further produce a WZ pair. $q_1\bar{q}_2 \rightarrow W \rightarrow WZ$

- **Single top**: Single top quarks are produced via weak interaction. Single top quarks are produced by three processes.

  1. t-channel: This involves the exchange of a space-like W boson. This process is also called W-gluon fusion, because the b-quark arises from a gluon splitting to bb.
  2. s-channel: This involves the production of a time-like W boson, which then decays to a top and a bottom quark.
  3. tW-channel: involves the production of a real W boson. In this process b-quark absorbs a gluon and then decayes to top quark and real W boson.

- **QCD multijets events**: Quarks and gluons emit many gluons while moving at high energies. These gluons get hadronised and form jets. These jets mimic as they are from the decay of a top quark and hence give a large back ground.

Different process mentioned above have W or Z or jets. W/Z decays to give quarks and leptons(Decay of W boson is discussed in section 2). So in the final states we get leptons and jets which mimic the decay products of top quark. To find the cross section and to improve the signal to background ratio of the selected sample we need to reduce the backgrounds by applying various selection on the data collected in experiments. First we study Monte Carlo samples of various processes and try to analyze the final states of each channel and on the basis of the outcome we apply selection criteria on the data.

Table 1. Total no. of events and event left after the triggering(Cut1) are given in column 2 and column 3 respectively. Column 4 and following columns give the efficiency of different cuts w.r.t to column 3 for various process(0.000 means efficiency of that cut is zero upto three decimals and 0 means no event is left after that cut).

Process	Total events	Cut1	Cut2	Cut3	Cut4	Cut5	Cut6	Cut7
$t\bar{t}$	36941	4515	0.862	0.829	0.784	0.131	0.039	0.036
Z + jets	77729	77729	0.935	0.850	0.412	0.000	0.000	0
Single top	5684	5684	0.896	0.857	0.838	0.020	0.004	0.003
W+Jets	109737	109737	0.868	0.811	0.811	0.000	0	0
WW	4580	4580	0.888	0.846	0.797	0.001	0	0
WZ	3367	3367	0.917	0.861	0.691	0.001	0	0
ZZ	2421	2421	0.951	0.897	0.417	0.000	0	0
QCD	142	142	0.105	0.077	0.077	0.014	0.007	0.007
Data	469384	469384	0.477	0.434	0.405	0.001	0.000	0.000

3.2 *Selection criteria and analysis*

1. Cut1- Only Muon Triggered
   We take only muon triggered events as our data from CMS. Muon triggering means an event will be stored only if the detector detects a muon in the final state. If there is no muon generation then event will be rejected.

2. Cut2- Isolation Criteria < 0.10
   A lepton produced in the decay of W (or Z) is not surrounded by other energetic particles which is opposite to the situation where in QCD process a lepton from the b quark decay ($\mathrm{b} \rightarrow \mathrm{c}\ell\nu$) will be surrounded by other particles. In the former case the lepton is isolated. For isolation we choose energy deposited by all particles within the 0.4 cone radius around muon with less than 10 % of p_t of muon.

3. Cut3- Leading Muon > 26 Gev
   In case of leptonic decay mode of W, it is a two body decay (lepton and neutrino). Neutrino and muon are massless compared to W, so all the energy of W (rest mass energy and kinetic energy if any) go in as the momentum of muon and neutrino. As the mass of W is around 80 GeV, the maximum momentum of muon is 40 GeV approx. By this selection we reduce the background due to less energetic muons coming from mainly QCD multijet events.

4. Cut4- No second lepton in the event
   In the semileptonic decay of $\mathrm{t\bar{t}}$ there is only one lepton so we need one lepton in the final

state. But in Z+jets , ZZ there are more than one lepton. So to reduce background due to these events we choose this criteria.

5. Cut5- Atleast 4 jets with $p_t > 30$ GeV
   In the semileptonic decay channel of $t\bar{t}$ there are two b-tag jets and two quark jets from W, in total 4 jets. But in Z+jets, ZZ there are not many events with 4 jets.

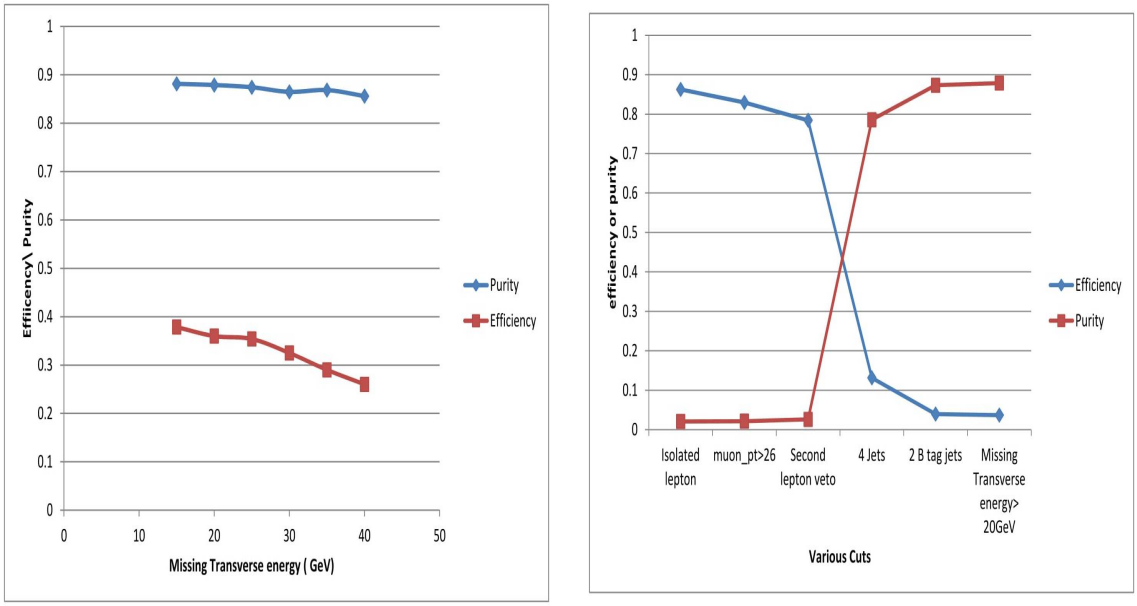

Figure 2. Left plot shows optimization of missing transverse energy and right plot shows how efficiency and purity is varying with various cuts applied. Efficiency is multiplied with the factor of 10 in the left plot.

6. Cut6- Exactly 2 b-tag jets
   We get b and $\bar{b}$ jets from t and $\bar{t}$ decay respectively. Now why exactly 2 b-tag jets? the answer is because we can get b- tag jet in single top event but it will give only one b tag jet. So exactly 2 b-tag jet reduce single top event.

7. Cut7- Missing transverse energy > 20 GeV
   True missing energy is due to the undetected neutrino. But due to detector resolution there may be non zero missing energy in the reconstructed event which do not contain any ν. Since we can't measure the longitudinal component of energy-momentum in the initial state of the hard scatter process, so we deal only with the transverse component. Missing energy is defined as negative of vector sum of all p_t. We choose only 20 GeV here because as missing energy threshold is increased efficiency is decreased but purity remains the same with some small fluctuations. So it is needed to optimize the efficiency and purity. Graph in Figure 2 shows

the variation of efficiency and purity with change in missing energy. Efficiency after various selection criteria is given in table 1.

3.3 *Determination of cross section*

$$\text{crosssection}(\sigma) = \frac{\mathrm{N_{signal}} \times \mathrm{Purity}}{\mathrm{L} \times \epsilon \times \mathrm{Br}}$$

Where the branching ratio (Br) of $\mathrm{t} \to \mu\nu\mathrm{b}$ = 13.4% , Br of $\bar{\mathrm{t}} \to \mathrm{q\bar{q}\bar{b}}$ = 66.5%
Br of $\mathrm{t\bar{t}} \to \mathrm{semileptonicmode} = 2\times$ Br of $\mathrm{t} \to \mu\nu\mathrm{b}\times$Br of $\bar{\mathrm{t}} \to \mathrm{q\bar{q}\bar{b}}$ = 17.82 %
$\mathrm{Purity} = \frac{\mathrm{N_{signal}}}{\mathrm{N_{total}}} = 0.878$ Integrated Luminosity (L) = 50 pb^{-1}
$\mathrm{N_{signal}} = \mathrm{N_{data}} - \mathrm{N_{Background}} = 43 - 1.155 = 41.845$

$$\mathrm{Efficiency}(\epsilon) = \frac{\text{total no. of signal events passing all cuts}}{\text{total no. of signal event after trigger}} = 0.036$$

$$\sigma = \frac{41.845 \times 0.878}{50 \times 0.036 \times 0.178} = 114.540\ \mathrm{pb}$$

Estimation of statistical error:

$$(\frac{\Delta\sigma}{\sigma})^2 = (\frac{\Delta \mathrm{N}}{\mathrm{N}})^2 + (\frac{\Delta \mathrm{P}}{\mathrm{P}})^2 + (\frac{\Delta \mathrm{L}}{\mathrm{P}})^2 + (\frac{\Delta\epsilon}{\epsilon})^2 + (\frac{\Delta \mathrm{Br}}{\mathrm{Br}})^2$$

$\Delta\sigma = 27.260$ pb $\sigma = 114.540 \pm 27.260$ pb

4. STUDY OF JETS FROM THE DECAY OF TOP QUARK

4.1 *Hadronic jets in the experiments*

Jets are the collimated bunch of particles (mainly hadrons) coming from the hadroniztion of quarks and gluons. It is mentioned earlier that top decays to W^+b and W^+ further decays to $q\bar{q}$ or $\ell\nu$. If decay mode is leptonic we can detect lepton using tracking detector and calorimeters. But when W^+ decays to quark we can't detect it directly because quarks are unstable and they get hadronised to give many hadrons which we can't resolve in detectors. We get these hadrons as a collimated bunch of particles and this is referred to as jets. From the study of kinematics of jets we can associate a jet from top quark decay.

As there are two quarks in decay of W^+(hadronic mode), we get two jets in the final state and in combination of b quark we get three jets from top quark. As aforementioned, $\mathrm{t\bar{t}}$ event has three decay modes so accordingly we get 2,4 and 6 jets for dileptonic, semileptonic and fully hadronic channels respectively.

In case of fully hadronic decay of $t\bar{t}$ we get 6 jets but this is true when the kinetic energy of top quark is low $i.e$ top quark is not boosted. At lower energy we are able to resolve the three jets on the detector. But when energy of top quark is very high, jets produced from decay of top are also

largely boosted. Hence these jets are very close to each other such that we are not able to resolve these jets and three jets appear as one fat jet. So at high energy when jets are close to each other it is needed to study the substructure of jet to associate a jet with the parent top. Figure 3 displays the cartoon of boosted jet.

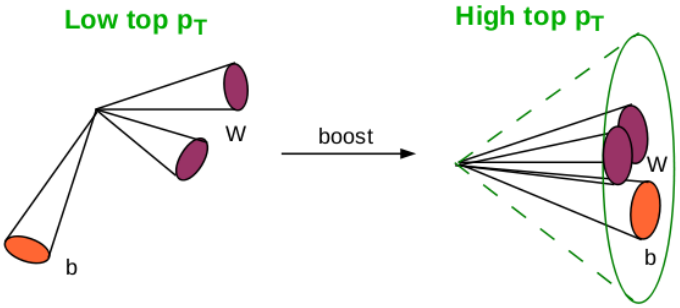

Figure 3. Conversion of three jets into a fatjet at high $\mathrm{p_t}$

4.2 *N-Subjettiness*

N-subjettiness is a variable designed to identify boosted hadronic decaying object like top quark. It is an effective discriminating variable for tagging boosted objects and rejecting the background of QCD jets with large invariant mass. It allow us to break the jets into subjets creating some imaginary axis. N-subjettiness is denoted by τ_{N}. Where 'N' stands for the number of subjets in a jet[1].

$$\tau_{\mathrm{N}} = \frac{1}{\mathrm{d_o}} \times \sum_{\mathrm{k}} \mathrm{p_{T,k}} \times \min[\Delta \mathrm{R_{1,k}}, \Delta \mathrm{R_{2,k}}, \Delta \mathrm{R_{3,k}}....., \Delta \mathrm{R_{N,k}}]$$

Here

$$\mathrm{d_o} = \sum_{\mathrm{k}} \mathrm{p_{T,k}} \mathrm{R_o}$$

k runs over the constituent particles in a given jet, p_T,k are their transverse momenta and $R_{J,k}$ is the distance in the $\eta - \phi$ plane between a candidate subjet J and a constituent particle k.

Jet with $\tau_{\mathrm{N}} \approx 0$ have all their particles aligned with the subjet directions and therefore have N subjets. Jet with $\tau_{\mathrm{N}} \gg 0$ have a large fraction of their energy distributed away from the subjet directions and therefore have at least N + 1 subjets. So the value of τ_{N} tells to what degree our estimated number of subjets in a fatjet is right.

4.3 *Analysis for substructure of top quark jet*

For analyzing the conditions at high energy in proton proton collision at LHC we generated top quark pair event using Pythia event generator with centre of mass energy of 14 TeV. When top quark

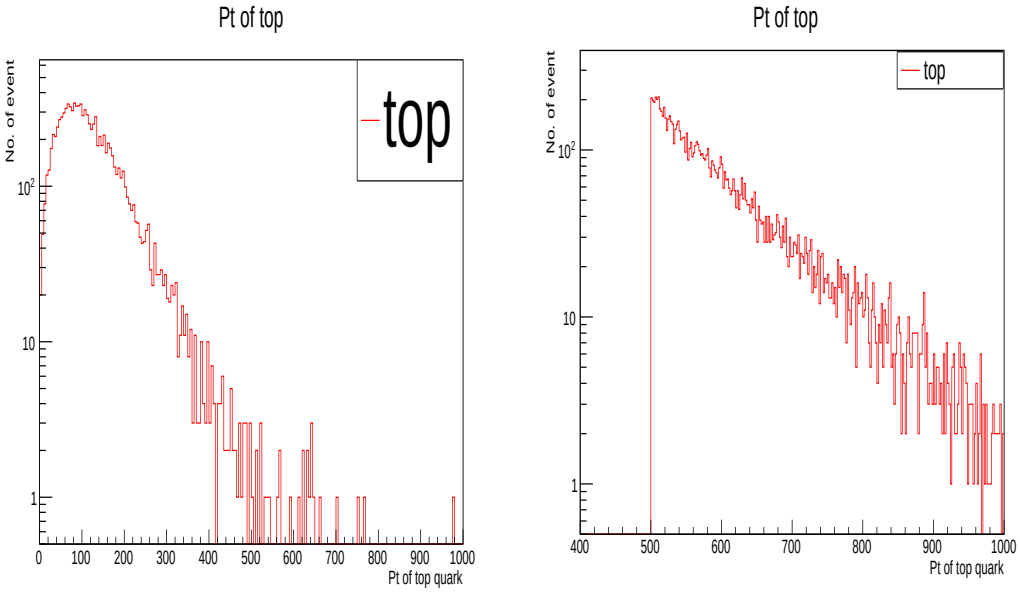

Figure 4. Above graph shows transverse momentum spectra of leading top quark in proton proton collision at 14 TeV. In the left graph it can be seen that number of events are decreasing very fast with increasing $\mathrm{p_t}$. There are much smaller number of events above 500 $\mathrm{p_t}$. Right graph shows the spectra of boosted top quark above 500 $\mathrm{p_t}$.

is generated it shows a distribution of p_t of top quark(Figure 4 left plot). As we are interested in highly boosted top quark we choose only high p_t top quark (eg. above 500 GeV). But as we apply this selection criteria, efficiency of sample become very low ~ 0.29 % .

To get a fair number of events for analysis and to get a good distribution we need to generate a larger no. of events when the p_T of the top quark is above 500 GeV. But to save computing power instead of generating a large sample we have forced top quark to have p_t more than threshold(500 GeV)(Fig 4 right plot). We have also forced the top quark to decay in fully hadronic channel.

At generator level we have full information of final state particles and we reconstructed jets from particles in the final state using Cambridge/Aachen algorithm of Fastjet [5],[6],[7],[8]. For jet clustering we choose radius of cone for fat jet from top quark equal to 1.5. With this we get only 65% jets of the generated top events (Fig 5). After constructing jets we use a standard tool called "top tagger" to find that if the jets are coming from top or from other particles. Now to find the substructure we use N-subjettiness method. For this we try to find no. of subjets by varing τ_N for $\mathrm{N} = 1, 2, 3$.

QCD multijet processes are the dominant source of boosted fat jets which can mimic hadronic decay of boosted top quark. So we follow the same procedure QCD events and results are shown in Figure 6 and Figure 7.

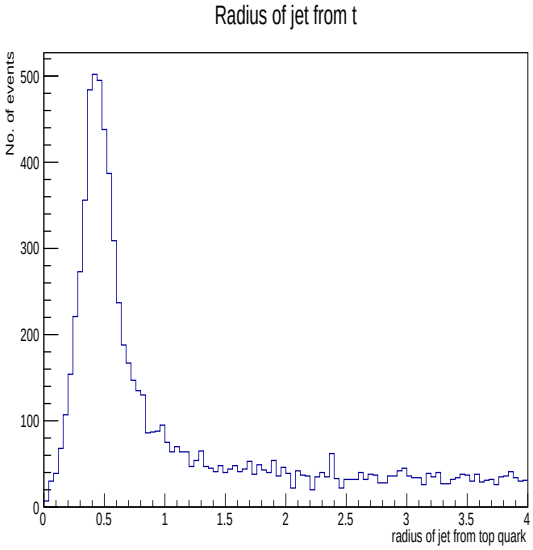

Figure 5. Radius of fat jet from top quark estimated by calculating the distance between b quark and W quark in $\eta - \phi$ space.

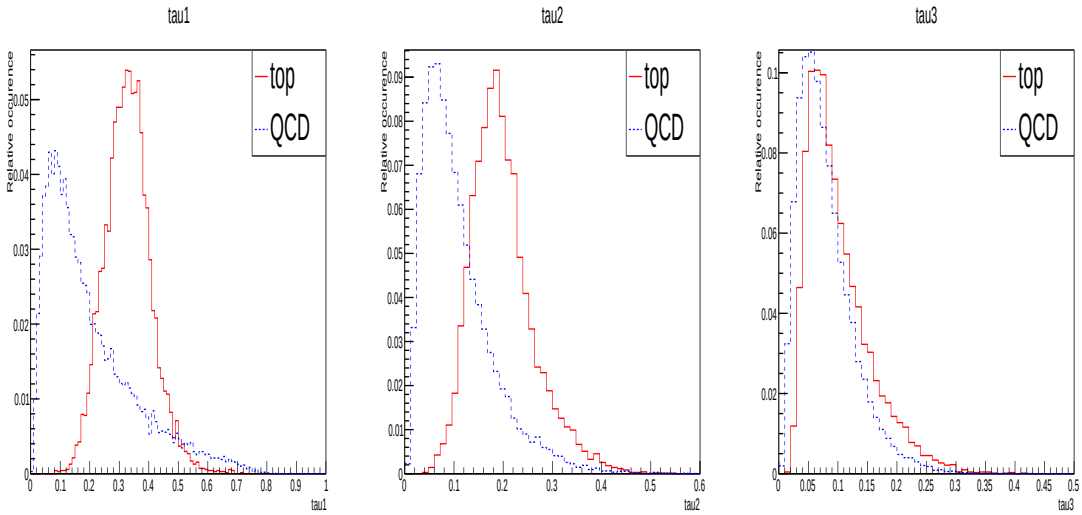

Figure 6: N-subjettiness of jet from top quark and QCD multijet events.

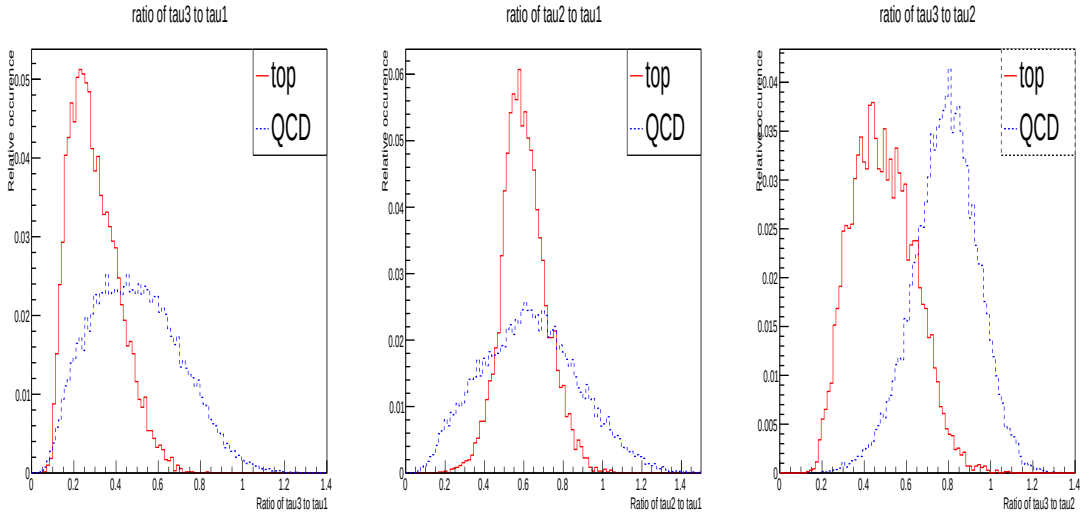

Figure 7: Ratios of N-subjettiness of jet from top quark and QCD multijet events.

4.4 *Observations*

- As the jets from top quark contain three subjets, so it give $\tau_1 \gg 0$(Fig 7 left plot). As we start increasing the number of subjets from one to three, peak of N-subjettiness starts shifting to lower value(Fig 7 middle and right plot). 3-subjettiness for three subjet is approximately equal to zero which confirms that boosted top jet has three subjets.

- In QCD events a boosted jet contains many subjets and these are distributed evenly in the fatjet and not like a top jet. So when we try to find N-subjettiness for QCD multijets it gives a peak near zero for τ_1, τ_2, τ_3. It can be seen from blue line in the graphs.

- When we calculate the ratio of these subjettiness it gives different results for top quark jet and for QCD multijets(Fig 7).

- By using the N-subjettiness variable and its ratios we can distinguish the QCD multijets and top quark events. We can reduce background by applying optimum cut on $\frac{\tau_3}{\tau_2}$.

5. ACKNOWLEDGEMENT

This project would not have been possible without the support of many people. Sarvesh Bansal would also like to thank his colleague Sarvesh Uplap for helping throughout the entire project. He would also like to thank Ph.D students Arvind, Pallabi and Bibhu Prasad for clearing many doubts and helping in project. He would also like to thank TIFR for providing such great opportunity.

6. REFERENCE

1. Jesse Thaler and Ken Van Tilburg,*Identifying boosted objects with N-subjettiness* [arXiv:1011.2268v3 [hep-ph] 25 Jan 2011]
2. T.M. Liss, F.Maltoni, and A. Quadt 2013,*The Top Quark*.
3. C. Clement Stockholm University, Fysikum, S-10691 Stockholm, Sweden, *Properties of the Top Quark*,SLAC Summer Institute on Particle Physics (SSI04), Aug. 2-13, 2004
4. Markus Cristin -ziani, Martijn Mulders,*Top-quark physics at the Large Hadron Collider*,Topical Review,[arXiv:1606.00327v2 [hep-ex] 4 Nov 2016]
5. Jet Algorithms,Vivians Meeting,Philipp Schieferdecker (KIT),April 17th 2009
6. Jet Reconstruction Journal Club 7/28/08
7. Stan Bentvelsen and Irmtraud Meyer,*The Cambridge jet algorithm: features and applications*,CERN-EP/98-043,March 11th, 1998,[arXiv:hep-ph/9803322v2 2 Apr 1998]
8. FastJet user manual, arXiv:1111.6097v1 [hep-ph] 25 Nov 2011

On Development Of Hydrogen Storage Material For Vehicular Application

Jyotsana Kala[1*]
M.Sc. 1st Sem, Department of Physics, Pt.L.M.S.Govt.P.G.College, Rishikesh (Autonomous College) Dehradun-249201, Uttarakhand

Abstract: Transportation is a major sector that consumes energy. At present 24.6% of total energy is consumed in transportation sector around the globe. In India, the percentage of total energy consumed in transportation is 15%. At present, the major fuel for transportation is fossil fuel, which produces a lot of pollution (carbon imprint) in the environment. Hence the society must move towards the use of electric vehicles or adopting a clean fuel for vehicle. Hydrogen is an alternate fuel which can be stored in a vehicle directly or in the form of negative electrode material of nickel metal hydride (Ni-MH) battery. In the hydrides some of the important parameters are the heat of formation and plateau pressure. Until now, the search of optimum material properties is based on trial and error method by substituting other elements in basic alloy. In the present study, a semi-empirical formula has been proposed to calculate the heat of formation of AB_5 - type multi-component hydrogen storage alloy. The formula has been applied to calculate heat of formation of binary hydrides, ternary hydrides and multi-component hydrides. Very good agreement with experimental values has been achieved. The heat of formation has also been correlated with the plateau pressure. This model will help in predicting important thermodynamic parameters of novel hydrogen storage materials.

Keywords: Metal hydride battery, Multicomponent metal hydride, Heat of formation.

1. INTRODUCTION

Hydrogen storage materials can be utilized in electric vehicles directly or in form of negative electrode material or nickel metal hydride (Ni-MH) battery [1, 2]. Heat of formation of hydride and plateau pressure of pressure-composition isotherm are important parameters of hydrogen storage material [3, 4]. One of the basic alloys for this application is $LaNi_5$ which is similar to $MnNi_5$. The hydrogenation properties of these two alloys do not fulfil all the requirements for specific applications. Therefore they need to be tailored. Till now, the search of appropriate material properties has been based on trial and error methods by substituting other elements in the basic alloy [5]. Although multi-component alloys offer better hydrogenation characteristics in comparison to basic alloys, no model is known to calculate heat of formation of hydrides of multi-component hydrogen storage alloy properly. In the present paper, a semi-empirical formula to calculate the heat of formation of AB_5 - type multi-component hydrogen storage alloy is proposed. This formula has been applied to calculate the heat of formation of binary hydrides, ternary hydrides and multi-component hydrides.

*jyotsanakala1@gmail.com

2. SEMI-EMPIRICAL FORMULA FOR HEAT OF FORMATION

To calculate heat of formation (ΔH) of a hydride, Van Mal et al. have given rules of reverse stability as given below [3]. ΔH for a ternary hydride AB_nH_{2m} can be given in terms of the ΔH values of associated binary compounds by the equation

$$\Delta H(AB_nH_{2m}) = \Delta H(AH_m) + \Delta H(B_nH_m) - \Delta H(AB_n) \quad (1)$$

2.1 Proposed formula for multi-component alloy

We want to consider a system where A and H_{2m} are fixed and make an alloy at the B site by substituting some of the B atoms by C atoms. The proposed semi-empirical formula of heat of formation of a multi-component hydride alloy $AB_{n-p}C_pH_{2m}$ is given by

$$\Delta H(AB_{n-p}C_pH_{2m}) = \Delta H(AH_m) + (1-x)\Delta H(B_nH_m) + x\Delta H(C_nH_m) - \Delta H(AB_{n-p}C_p) \quad , \quad (2)$$

where $x = \frac{p}{n}$ and p takes values $0,1,\ldots,n$.

This equation interpolates between $\Delta H(AB_nH_{2m})$ and $\Delta H(AC_nH_{2m})$ when p takes values from 0 to *n* i.e. x goes from 0 to 1. The heat of formation of the ternary $AB_{n-p}C_p$ can be interpolated between the corresponding values for the binary compounds AB_n and AC_n using the equation

$$\Delta H(AB_{n-p}C_p) = (1-x)\Delta H(AB_n) + x\Delta H(AC_n) \quad (3)$$

Most of the time the values of the heat of formation of binary hydrides AH_m, B_nH_m and C_nH_m, for general values of *m* are not known, but the values for AH_3, B_nH_3 and C_nH_3 etc. are known. We suggest a simple equation to get the unknown values as

$$\Delta H(AH_m) = \left(\frac{m}{3}\right)\Delta H(AH_3);\ \Delta H(B_nH_m) = \left(\frac{m}{3}\right)\Delta H(B_nH_3);\Delta H(C_nH_m) = \left(\frac{m}{3}\right)\Delta H(C_nH_3) \quad (4)$$

2.2 Calculation of heat of formation of alloy hydrides using equations 2, 3 and 4

Based on the calculation from above mentioned equations 2, 3 and 4 following results have been obtained.

Table 1. Heat of formation **(H)** of binary hydrides in units of kcal/mole and verification of proposed Eq. 4.

No.	Compound	Heat of formation Reported	Reference of reported value	Heat of formation calculated using Eq. 3
1.	LaH_3	-60	3	-
2.	LaH_2	-49.6	3	-40
3.	Ni_5H_3	+1.0	3	-
4.	Ni_5H_2	+0.7	3	0.67
5.	Co_5H_3	+7	3	-
6.	Co_5H_2	+5	3	4.67

Table 2 - Heat of formation **(H)** in units of kcal/mole of ternary and multi-component alloy and verification of proposed Eq. 3.

No.	Compound	Reported value of Heat of formation	Reference of reported value	Heat of formation calculated using Eq. 3
1.	$LaNi_5$	-40	3	-
2.	$LaCu_5$	-24.0	4	-
3.	$LaCo_5$	-17.5	3	-
4.	$LaFe_5$	+4	3	-
5.	$LaCr_5$	+12	3	-
6.	$LaAl_5$	-44.4	4	-
7.	$LaMn_5$	+1.2	4	-
8.	$LaNi_4Cu$	-34.2	4	-36.8
9.	$LaNi_4Co$	-		-35.5
10.	$LaNi_4Fe$	-31.0	4	-31.2
11.	$LaNi_4Al$	-40.6	4	-40.88
12.	$LaNi_4Mn$	-32.0	4	-31.64
13.	$LaNi_4Cr$	-		-29.6

Table 3- Heat of formation **(H)** in units of kcal/mole H_2, of ternary and multi-component hydrides as calculated through proposed Eq. 2.

S. No.	Alloy	Heat of formation Reported	Reference of the reported value	Heat of formation Calculated
1.	$LaNi_5H_6$	-7.3	4	-6.33
2.	$LaNi_4CoH_6$	-7.56	4	-7.43
3.	$LaNi_4CuH_6$	-8.1	4	-8.068
4.	$LaNi_4FeH_6$	-8.2	4	-8.87
5.	$LaNi_4CrH_6$	-10.2	4	-10.0
6.	$LaNi_4MnH_6$	-11.6	4	-11.6
7.	$LaNi_4AlH_6$	-11.4	4	-13.1

In summary, a good agreement can be seen in the calculated and reported values of heat of formation of multi-component hydrogen storage alloy using Eq. 2, 3 and 4 in Tables 1, 2 and 3.

3. ACKNOWLEDGEMENT

Author is grateful to Dr.Sumita Srivastava, Associate Professor, Department of Physics, Pt.L.M.S.Govt.P.G.College, Rishikesh (Autonomous College) for helpful discussions.

4. REFERENCES

[1] S. Srivastava and R.K. Upadhyaya, "Investigations of AB_5-type negative electrode for nickel-metal hydride cell with regard to electrochemical and microstructural characteristics", *J. Power Sources* **195,** 2996 (2010).

[2] S. Srivastava and R.K. Upadhyaya, "Investigations of AB_5-type hydrogen storage materials with enhanced hydrogen storage capacity", *Int. J. Hydrogen Energy* **36**, 7114 (2011).

[3] H.H.Van Mal, K.H.J. Buschow and A.R. Miedema, "Hydrogen absorption in $LaNi_5$ and related compounds: experimental observations and their explanation", *J.Less Common Metals.* **35,** 65 (1974).

[4] A. Pasturel and C. Chatillon-Colinet, "Thermodynamic properties of $LaNi_4M$ compounds and their related hydrides", *J.Less Common Metals.* **84,** 73 (1982).

[5] M. H. Dhaou, S.Belkhiria, N. Sdiri, A. Mallah, S. Al-Thoyaib, A. Jemni and S. B. Nasrallah, "Thermodynamic and electric study of the $LaNi_{3,6}Al_{0,4}Co_{0,7}Mn_{0,3}$ alloy", *Int J Hydrogen Energy* **42**, 2209 (2017).

Positron Anhilation Spectroscopic Studies of Sr-substituted Lanthanum Ferrite $(La_{1-x}Sr_xFeO_3)$

Aparna Tomar[1]*
[1]M.Sc Physics (Final Year), Department of Physics and Astrophysics, University of Delhi, India.

Abstract. Lanthanum Ferrite is a pervoskite ferromagnetic insulator with wide areas of applications such as electrode material in solid oxide fuel cells, gas sensors and in high temperature atmspheric studies.However, achieving cent percent success of substitution is always a challenge. Incomplete substitution can result in a high concentration of structural defects like of Lanthanum by Strontium. The effects of vacancies on different physical properties have been investigated by different types of probes which unfortunately have not been able to yield conclusive results. Positron annihilation spectroscopy (PAS) is a well established spectroscopic probe to investigate defects. Its success in the investigation of defects and defect-related processes in a variety of solids has enriched the subject of solid state physics. Over the years, it has been recognized as the most sensitive and reliable among analytical probes that provide information on defects. In the present work, this technique has been used to extract information on the effects of substitution of La by Sr ions in $LaFeO_3$. The results are discussed in detail.

Keywords: Ferrites, Defects, Positron annihilation.

1. INTRODUCTION

1.1 *Positron Lifetime Measurement*

Positron being an antiparticle of electron, its lifetime and stability are very short. Whenever it comes in contact with an electron, it gets annihilated. The processes involved during the annihilation are discussed below.

The process starts with the decay of the radioactive sources like the one used in this work Na^{22} isotope emitting a positron and the daughter nucleus (Na^{22}, in this case) transiting from its excitation level to the ground state with the prompt emission of the difference in energy (1.276 MeV, in this case) as a gamma ray. This gamma ray serves as the birth signal of the positron. There is an emission of two gamma rays after the annihilation of the positron with energy 0.511MeV each, either of which serves as the death signal of the positron. The time interval between these two signals is called the lifetime of the positron.

The annihilation of positrons is directly related to the density of electrons at the site of annihilation.

*aparnatomar7@gmail.com

The decay rate of positron is given by [1]

$$\lambda = \pi r_0^2 c \zeta n_e \tag{1}$$

where r_0 is the classical electron radius, c the velocity of light and ζ is the enhancement factor which accounts for the local increase in the density of electrons (n_e) due to Coulomb attraction by the positron. The equation determining ζ is given as

$$\zeta = 1 + 1.23r + 0.8295r^{\frac{3}{2}} - 1.26r^2 + 0.3826r^{\frac{5}{2}} + 0.167r^3 \tag{2}$$

where r is the radius of a sphere whose volume equals the average volume per conduction electron of the solid. Also, $\lambda = \dfrac{1}{\tau}$where τ is the positron lifetime.
In solid containing defects, the annihilation of positrons is governed by the following rate equations.

$$\frac{dn_b}{dt} = -\lambda_b n_b - \kappa_d n_b \tag{3}$$

$$\frac{dn_d}{dt} = -\lambda_d n_d + \kappa_d n_b \tag{4}$$

where n_b is the number of positrons in the bulk n_d is the number of positrons in the defects at any instant of time t and κ_d is the rate of trapping of positrons from the bulk into the defects.
The above two equations are solved to give positron lifetime spectrum as

$$N(t) = n_b + n_d = I_1 \exp\left(\frac{-t}{\tau_1}\right) + I_2 \exp\left(\frac{-t}{\tau_2}\right) \tag{5}$$

where, for simplicity we define the following relations between the various useful physical parameters.

$$I_1 = \frac{\lambda_b - \lambda_d}{\lambda_b - \lambda_d + \kappa_d} \tag{6}$$

$$I_2 = \frac{\kappa_d}{\lambda_b - \lambda_d + \kappa_d}$$

Further it can be shown that $\tau_1 = (\lambda_b + \kappa_d)^{-1}$ and $\tau_2 = \lambda_d^{-1}$ It may be further noted that $I_1 + I_2 = 1$, $i.e., 100\%$ when the relative intensities are expressed in percentage.

1.2 *Coincidence Doppler Broadening Spectroscopic Measurements*

Whenever electron-positron annihilation takes place, two gamma rays each of energy 0.511 MeV are emitted in the opposite directions. The positron loses its kinetic energy and linear momentum to the material due to inelastic collisions through several energy dissipative processes whereas the annihilating electron has a finite linear momentum. Therefore, according to the law of conservation of linear momentum, the total momentum after the annihilation cannot reduce to zero. Hence the gamma rays will be moving away from each other with a slightly different direction and also the energies will be shifted by magnitudes $E_{\gamma 1} - E_{\gamma 2} = 2\Delta E = p_L c$ which gives $\Delta E = \dfrac{p_L c}{2}$,

where p_L is the longitudinal component of the electron momentum. This shift in the energies of the gamma rays is known as Doppler shift [1]. It gives an overall broadening to the 0.511 MeV gamma ray spectrum and it is monitored and the changes as functions of the changing parameters of the samples are carefully evaluated.

1.3 *Angular Correlation*

There is a loss of the kinetic energy and hence the linear momentum of the positron when it enters a material, by virtue of processes likes electronic excitation, ionization of atoms, phonon interaction and plasmon excitation. Conservation of linear momentum demands that the non-zero momentum of the electron needs to be conserved. Hence, the two gamma rays move apart making an angle (θ) with the axis passing through the sample and the detector. The annihilation cross section (σ) given by Eq. (7) below dominates over the other processes only at very low velocities (v) of the positron

$$\sigma = \frac{\pi r_0^2 c}{v} \tag{7}$$

As already mentioned, in order to conserve the linear momentum, the annihilation gamma rays move in opposite directions with an angle θ, which is given by the equation

$$\theta = \frac{p_z}{m_0 c} \tag{8}$$

where m_0 is the mass of either the electron or the positron. The momentum distribution in two dimensions (p_y and p_z) can also be recorded in this way in two-dimensional angular correlation of annihilation radiations (2d-ACAR) measurements.
Angular correlation studies have not been carried out in the present work being reported here.

2. EXPERIMENTAL DETAILS

The positron lifetime spectra were recorded using a slow-fast gamma ray spectrometer [2]. The data was analyzed using the PALSfit program [3]. This is done in two stages, RESOLUTIONFIT and POSITRONFIT. In RESOLUTIONFIT, the program is used to calculate the instrumental resolution function which consists of a number of Gaussians with respective FWHMs, intensities and displacements and deconvolutes it from the recorded positron lifetime spectrum. The resultant spectrum, after the background subtraction, is a true multi exponential decay spectrum. The POSITRONFIT program is then used for fitting the resultant spectrum with a number of decaying exponentials and also incorporates the source correction for contributions from the source backing materials which otherwise interfere with the spectrum of the samples. The program continues the iteration procedure till the best reduced chi-square is obtained. Typically values between 0.9 and 1.2 are accepted as good fit. The corresponding positrons lifetimes and intensities are considered as the final results. The coincidence Doppler broadening spectroscopy data are analyzed with the help of the OriginPro 8.5 software.

3. RESULTS AND DISCUSSION

3.1 *Results of analysis of positron lifetime spectra*

The peak normalized positron lifetime spectra of all the samples are shown in Fig. 1. The nature and shape of the curves indicate the multi exponential decaying nature of the spectra and which is a clear evidence to the presence of large positron lifetimes. The large positron lifetimes within the samples show the presence of defects in the samples. The positron lifetimes and intensities obtained from the PALSfit analysis are given in Table 1.

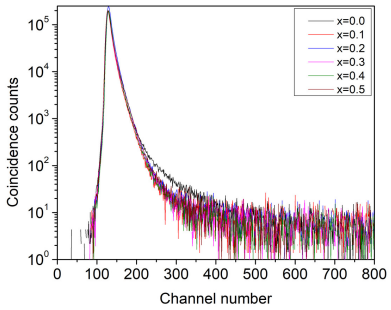

Figure 1. Peak normalized positron lifetime spectra of the samples

The nature of variation of the different positron lifetime parameters with different concentration of Sr is rather smooth and makes the interpretations easy and straightforward. The initial decrease of τ_1 is due to the diminishing contribution of positron annihilation in the bulk, which happens when more number of positrons are trapped in defects. For this to happen, the defect concentration needs to have increased. This is confirmed by the increase of the intensity I_2 at this stage.

Table 1: The positron lifetimes and relative intensities obtained from the PALSfit analysis and the calculated mean lifetime and the bulk lifetime in the different samples.

Concentration of Sr^{3+}	τ_1(ns)	τ_2(ns)	τ_3(ns)	$I_1(\%)$	$I_2(\%)$	$I_3(\%)$	τ_m(ns)	τ_b(ns)
0	0.1434	0.4781	2.7979	87.6567	11.3974	0.9459	0,20666	0.15737
0.1	0.131	0.3604	3.9904	75.066	24.6401	0.2939	0.19887	0.15589
0.2	0.1383	0.3838	3.9628	76.0649	23.6214	0.3137	0.20829	0.1635
0.3	0.1452	0.401	4.2581	78.1673	21.5506	0.2821	0.21193	0.16888
0.4	0.1437	0.3825	4.6498	79.2838	20.4311	0.285	0.20533	0.16523
0.5	0.1417	0.3725	3.0733	67.4171	32.0733	0.3947	0.22713	0.17793

The sharp decrease in τ_2 in the initial stages of strontium incorporation indicates a reduction in

the sizes of the vacancy type defects which trap positrons. One more reason for the substantial drop in τ_2 can be as follows. Initially, in the undoped sample, the positrons were able to diffuse till the surfaces of the nanocrystallites and get annihilated on the surfaces. But, complete replacement of La^{3+} with Sr^{2+} does not take place and, on the other hand, as we keep on increasing the percentage of doping, this factor keeps on decreasing. The process also results in the formation of vacancies with virtual negative charges and the positrons are strongly trapped in these vacancies and get annihilated before reaching to the surface.

The intensity I_2 shows a sharp increase which indicates that additional defects are created due to non-occupancy of the vacant lattice sites by the ions of the elements with which doping is done. Thus, we see more defects in doped sample as compared to undoped one.

The behaviour of τ_3 and I_3 are explained as follows. This lifetime and intensity is due to the formation of orthopositronium atoms in the intercrystalline regions. Orthopositronium is a metastable bound state of an electron and a positron with their spins oriented in the same direction to give a triplet configuration. The annihilation of orthopositronium in a material normally occurs through the pick-off process where an electron with opposite spin takes away the positron and forms the spin singlet parapositronium, which has a much reduced lifetime. The effective lifetime is therefore a few nanoseconds only. The increase is basically due to the increase in the intercrystallite separation. This happens when cations of higher radii are doped to replace existing host cations. Due to the increased ionic radii, strain is developed within the crystallite. One way to get rid of the strain is to accommodate the substituted cations at sites closer to the surfaces of the crystallites. As concentration of substitution is increased, more ions are to be accommodated at the surfaces. This implies more surfaces are required and hence the sizes of the crystallite are reduced to enhance the surface to volume ratio. As the crystallite sizes are reduced, their separation increases and is reflected in the increase of τ_3.

The decrease in I_3 is explained as follows. The actual substitution decreases on increase in the known incorporated substitution and hence we have more number of free Sr^{2+} ions in the intercrystallite region and hence it reduces the probability of positronium formation.

Both the mean positron lifetime and the bulk positron lifetime increases with substitution. The increase of τ_m reflects the dominance of τ_3 which increases due to the increase in the intercrystallite separation. The reason of the increase in τ_b is not clearly understood at this stage but will be discussed elsewhere.

3.2 *Coincidence Doppler Broadening Measurements*

For Doppler Broadening measurements, energy sensitive detectors with high energy resolution are required. So we have used High Purity Germanium detectors (HPGe) with an energy resolution of

about 1.3 keV at 0.511 MeV. The HPGe detectors are operated with the crystal at liquid nitrogen temperature to minimize the leakage of current due to thermally generated charge carriers. A digitally stabilized multi-channel analyzer (MCA) has also been used for data acquisition and storage. The signal is generated here through the process of electron-hole pair production by the absorbed gamma ray energy and collecting the charge carriers so produced across an electric field by giving high operating voltages to the detectors. The signals are then processed using a series of nuclear electronic modules like timing filter amplifiers (TFAs), constant fraction discriminators (CFDs), delays, a TAC/SCA, gate and delay generator (GDG), linear gate and stretcher (LGS) etc. The signals from the GDG+LGS serve as the master-gate for the amplifier signals to get registered within the multichannel analyzer (MCA). The advantage in using the coincidence system is that the high nuclear gamma ray background which may submerge the core electron momentum events can be almost fully eliminated.

The ratio curves of the CDB spectra are generated by dividing the one-dimensional projection of the events parallel to the $\Delta E = E_1 - E_2$ axis within a window of $1.022 + / - 0.00087$ MeV with the corresponding spectra of pure and defect-free aluminium and are shown in Fig. 2(left). The prominent peak around $p_L(10^{-3}m_0c) = 9.66$ indicates the annihilation of positrons with the $2p$ electrons of oxygen ions [4]. This means positrons are getting trapped at the vacancies of the cations. As vacancies of the La^{3+} and Fe^{3+} cations are negatively charged, positrons will be strongly attracted towards these vacancies.

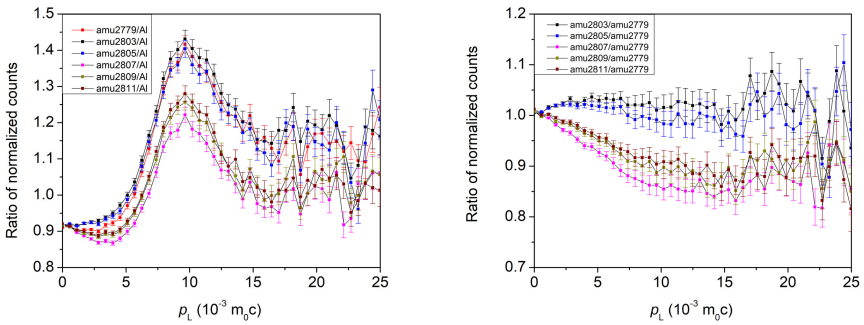

Figure 2. The ratio curves generated from the CDB spectrum of the samples with respect to reference aluminium (left) and the $x = 0$ samples (rightF).

On the other hand, since the vacancies of the O^{2-} ions are positively charged, positrons will be repelled by these vacancies. Still, in order to see the effect of substitution, another set of ratio curves are generated with the $x = 0$ sample as reference and these results are presented in Fig. 2(right). The curves are showing a broad peak around $p_L(10^{-3}m_0c) = 1216$ which perhaps indicates the substitution effects [4].

The CDBS peak ratios at $p_L(10^{-3}m_0c) = 9.66$ plotted against the doping concentration (Fig.

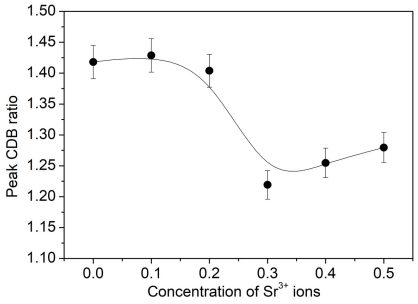

Figure 3. The CDBS peak ratios at $p_L(10^{-3}m_0c) = 9.66$ plotted against the doping concentration of strontium ions.

3) shows a drastic decrease between 0.2 and 0.3, which indicates the effects of substitution. There should have been a continuous increase due to the increase in defect concentration (as indicated by I_2). The fact that the CDBS peak ratio decreases indicates a reduction of positron trapping in cationic vacancies. In other words, some of the cationic vacancies are indeed getting occupied by strontium ions.

4. SUMMARY AND CONCLUSION

In this work, we have carried out positron lifetime and CDBS measurements on $LaFeO_3$ samples in which La^{3+} are progressively substituted by Sr^{2+} ions. We have been able to show from this study that the evolution of structural changes in the parent compound with changes in external parameters such as doping concentration can be directly seen through positron annihilation measurements. While it is always desirable to support the findings through other techniques such as X-ray diffraction, PAS studies can give information on certain aspects of substitutions.

We summarize the main parts of our findings.

- Up to $x = 0.4$, a number of fresh vacant lattice sites are being created as a significant fraction of the replaced La^{3+} sites are not getting occupied by the Sr^{2+} ions due to the mismatch of the ionic radii of La^{3+} and Sr^{2+}.

- Positronium formation within the intercrystallite region is significantly reduced on introducing Sr^{2+} ions due to dispersion of a fraction of them in the intercrystallite region. At the same time, due to the increase in the intercrystallite separation, the lifetimes of positronium increases. The decrease in crystallite sizes occurs due to strain minimisation through a process of near-surface atomic substitution that necessitates an increased surface to volume ratio and consequently a decreased crystallite size.

- Above $x = 0.4$, it is conjectured that additional phases are being formed because of which the positronium lifetime drastically reduces. We need to perform complementary experiments like XRD or transmission electron microscopy (TEM) to confirm these arguments.
- The results from CDB experiments also support these findings.

In conclusion, the substitution of La^{3+} ions by Sr^{2+} ions results in the creation of more defects in the compound due to ionic radii mismatch. However, it is still possible to alter the properties for better use and applications. Beyond $x = 0.4$, it is advisable to restrict the substitution of the parent compound and explore improved methods of reducing the defect concentration and the phase instabilities.

5. ACKNOWLEDGEMENTS

I wish to express my sincere gratitude to my supervisor, Dr. P.M.G. Nambissan, Applied Nuclear Physics Division, Saha Institute of Nuclear Physics, Kolkata for his valuable support and guidance throughout my project work. We both are further grateful to Dr. S. Asad Ali of Department of Applied Physics, Aligarh Muslim University, Aligarh, U.P. for providing us with samples used in this work. I also pleasantly acknowledge the atmosphere and assistance provided by the fellow project students Ms. Diksha Garg of my college, Ms. Ankita Kakoti of Cotton College, Assam and Mr. Akhil P.M. of R.V. College of Engineering, Bangalore.

6. REFERENCES

[1] R.W. Siegel, Annual Review of Material Science 10, 393-425 (1980).
[2] P.M.G. Nambissan, Nanotechnology: Synthesis and Characterization (Volume 2), eds. Shishir Sinha, N.K. Navani and J.N. Govil, Studium Press LLC, Houston, U.S.A. 2013, ch. 16, pp. 455 -491.
[3] J.V. Olsen, P. Kirkegaard, N.J. Pedersen and M. Eldrup, Phys. Status Solidi C, 2007, 4, 4004-4006.
[4] Increased elemental specificity of positron annihilation spectra. P. Asoka-Kumar, M. Alatalo, V.J. Ghosh, A.C. Kruseman, B. Nielsen and K.G. Lynn, Phys.Rev. Lett., 77(10): 20972100 (1996).

Synthesis of Ni-Fe-Al Heusler alloys and study of their microstructure and FSMA nature

Kuldeep Kargeti[1*], Ankit Kargeti[2] and PK Mukhopadhyay[3]

[1] M.Sc. II Sem. (Physics), School of Physical Sciences, Doon University, Dehradun
[2] M.Sc. IV Sem. (Physics), Invertis Institute of Applied Science and Humanities, Invertis University, Bareilly
[3] Laboratory of Condensed Matter Physics, SN Bose National Centre for Basic Science, Kolkata

Abstract: Ferromagnetic shape memory alloys (FSMA) exhibit Austenite – Martensite phase transformation which is a diffusionless structural transformation from a high temperature cubic phase to a lower temperature lower symmetry phase, like orthorhombic, monoclinic etc. These structural transformations are generally studied through resistivity, magnetization etc measurements. In this paper we discuss the results of our work on a Ni based FSMA alloy having composition $Ni_{60}Fe_{19}Al_{21}$ in order to find the shape memory effect closer to the room temperature. This compound can be a very useful substitute for other present systems in the category of smart materials. In addition to the conventional methods, we have also investigated the microstructure, AC resistivity as well as magnetic properties of this compound.

Keywords: Shape memory alloy, Smart materials, Microstructure, Heusler alloys.

1. INTRODUCTION

1.1 *Heusler Alloys*

Heusler alloys are inter-metallic compounds with fcc structure characterized by the chemical formula X_2YZ (Full Heusler alloy) and XYZ (half Heusler alloy), where X and Y are transition metal atoms and Z lies in the p-block of the periodic table. These alloys exhibit ferromagnetism, anti-ferromagnetism, superconductivity, thermoelectricity and magneto resistance. The first Heusler compound was discovered by the German scientist Heusler in 1930, who showed that in these compounds or alloys, magnetism varies with heat treatment. Some of the Heusler alloys show the properties of Ferromagnetic Shape Memory Alloys (FSMA). These are composed of Ni, Mn, Ga, Al, Fe, Co, Ge, Pd (like Ni_2MnAl, Ni_2MnGa, Ni_2MnIn, Ni_2MnSn, Ni_2MnSb, where Ni is X, Mn is Y, and Al, Ga, In, Sn, Sb are Z). The size and shape of FSMA can be altered by an external magnetic field. (see reference [1-16])

1.2 Ferromagnetic Shape Memory Alloys

When the temperature of the martensitic phase is increased, it converts into the Austenite Phase; this transformation involves a transition from the tetragonal structure of the martensitic to the cubic structure of the austenite (See Figure 1). Ferromagnetic Shape Memory (FSM) effect usually occurs in the low temperature Martensitic phase of the alloy. FSMAs undergo changes in their original structure when placed in an external magnetic field or alternatively by the effect of heat. For example, the shape of a FSMA changes in the presence of an external magnetic field and the original shape is recovered when the field is removed. A similar effect also occurs under heat treatment. The recovery

*kuldeepkargeti@gmail.com

of the original shape by cooling or removal of the magnetic field occurs because the low temperature

structure of FSMA has twin variants. During the application of magnetic field, as is common in several magneto elastic smart materials, there occurs simultaneous rotation of magnetic moments and reorientation of twin variants, (refer to the Figure 1). In the presence of external magnetic field, the boundaries between the variants are shifted and the domains align along one direction. When the magnetic field is removed the original domain structure reappears.

Magnetic anisotropy (MI) plays a crucial role in determining the energy required to change the magnetic structure in FSMA. The strength of MI determines the maximum strain associated with the FSMA property and which can be used for applications like actuators, sensors, memory devices, magnetic cooling systems and next generation material for aerodynamics.

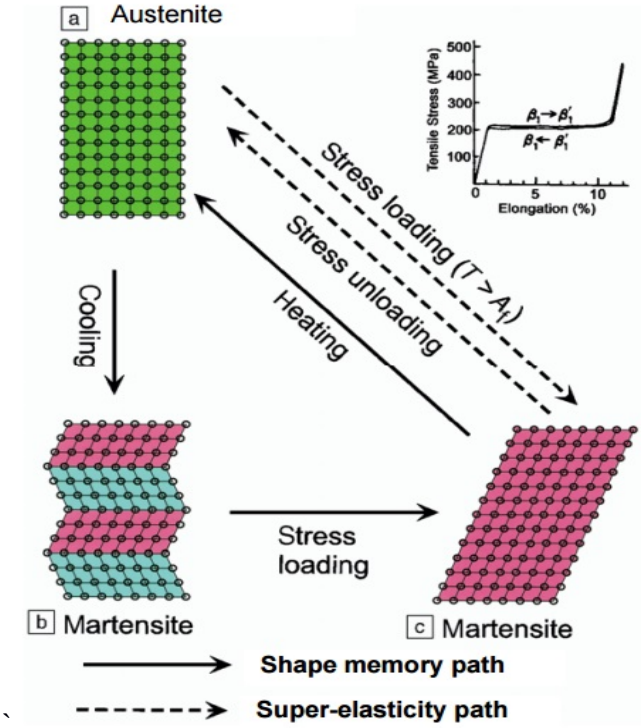

Figure 1–Schematic diagram showing the phase transformation of FSMA

2. SAMPLE PREPARATION

2.1 *Weighing And Cutting*

Approximately 2 grams of polycrystalline $Ni_{60}Fe_{19}Al_{21}$ alloy was prepared using an Arc melting furnace. High purity of raw elements Nickel (99.99%), Fe (99.99%) and Al (99.99%) were used. For this sample, Ni is around 1.3684 gm, Fe is around 0.4163 gm and Al is around 0.2217 gm. The sample is cut by Stanley Bolt cutter.

2.2 *Melting*

The alloy is melted in a Vacuum Arc Melting Furnace (See Figure 2). First we cleaned the glass chamber by acetone and then we made vacuum inside chamber (glass) around 10^{-3} pa. Then the weighed sample was kept on a copper crucible and was melted in an arc furnace three times under the flow of argon gas. The system was simultaneously cooled by the chilling water. The reason for melting three times is to improve the homogeneity of the alloy.

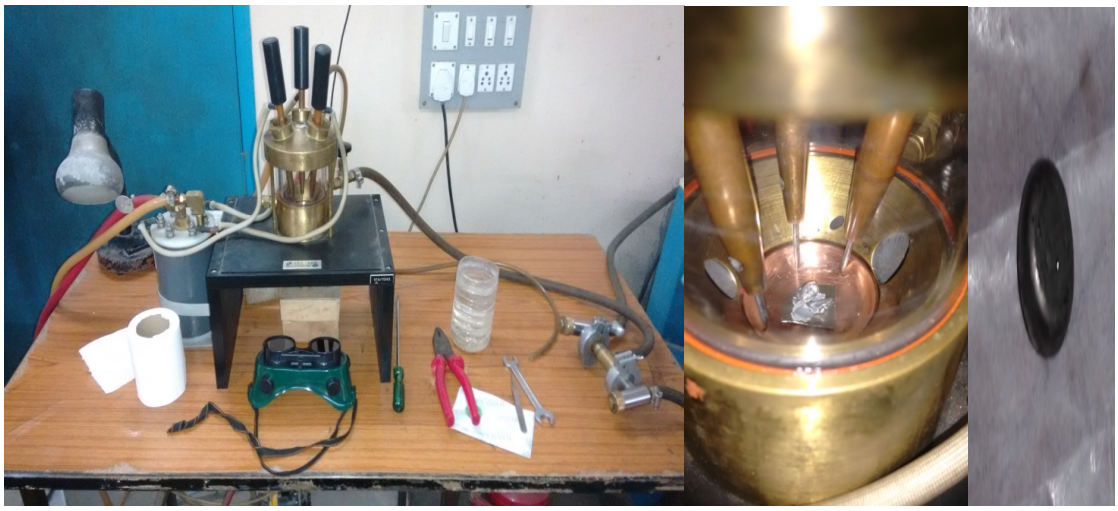

Figure 2-Vacuum Arc Melting Furnace set up and copper hearth

2.3 Cutting, Annealing, Polishing

Next step is to cut the arc melted sample into three parts using an anisomet diamond cutter, which took approximately 5 to 6 hours under a constant rpm (3rpm). The three parts were then polished with a polishing machine for nearly 2 hours for each part. Then two parts are put in a sealed Quartz ampule for heat treatment to increase the homogeneity of the sample further. The next step is to anneal the sample at 1000^0C for 48 hours. This is done through a resistive furnace whose temperature is fixed at the desired value for a given prescribed time. This is followed by a rapid quenching in cooled water. This was necessary to decrease the amount of undesired gamma phase and to give better results in our experiments. The annealed sample is then polished with the help of a polishing machine for 1 hour approximately for both the parts. The sample is then placed over the polishing cloth which is rayon fine and 1 micron in grit size, and chromium oxide powder was used to remove the dust from the sample surface. This is needed to get a more shinier surface as well as to get sharp edges. Now the sample is ready for different characterization experiments.

3. SAMPLE ANALYSES:

3.1 *Resistivity Measurement*

Resistivity measurement is done through a custom designed four-probe setup starting from a low temperature of 100 K to a maximum temperature of 300 K. This experimental set up consists of the four probe arrangement, sample holder, constant current generator, power supply and digital screen for measuring voltage and current across the probes (See Figure 3).

Since the resistivity ρ is R*A/ L, we measured the length L of the sample as 2.5 mm, width of the sample as 0.8 mm (area A is 2.00 mm^2). From the experiment we found the resistance R of the sample with current fixed at AC frequency of 111.11 Hz and Voltage around 5 Volts with the known standard resistance 35.5Ω. The values of the ρ is obtained as a function of temperature ranging from 4K to 300K.

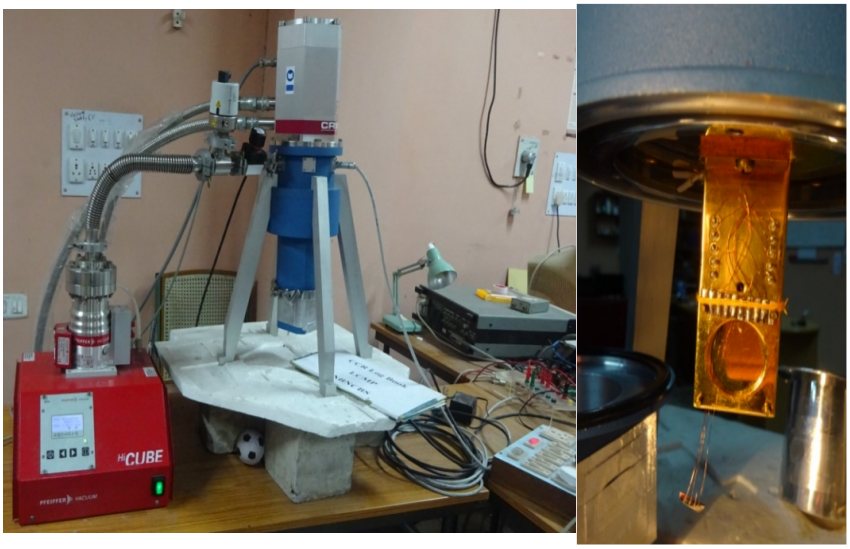

Figure 3. Indegenously designed set up to measure resistivity using ac four probe method

3.2 *XRD Measurement*

One part of the sample is used for the XRD Measurement, carried out by Rigaku X-Ray Diffractometer at 2deg/min. The measurements were carried out from 10 to 90 degrees, which is based on Bragg's diffraction equation $2d \sin\theta = n\lambda$, where the angle θ is the diffraction angle and λ is the wavelength of the x- ray beam and d is the spacing between the two atomic layers.

3.3 *FESEM*

FESEM is Field Emission Scanning Electron Microscope, which is used to characterize the topological details of a fractured surface. It has a range of imaging from 100 μm to 5μm, which is quite good for surface analyses.

4. RESULT

4.1 *Data Analyses*

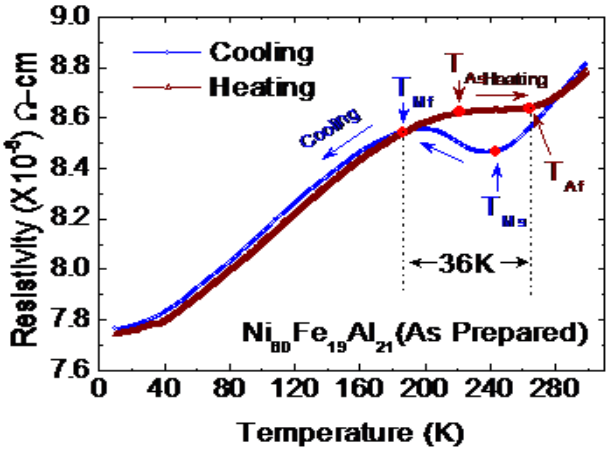

Figure 4 – Structural transformation under the temperature changes.

In Figure 4, we show the temperature dependence of resistivity in the range from 4K-300K. We find the austenitic to martensitic transition while heating and Martensitic transformation while cooling. The Martensitic transformation process starts below the room temperature at M_s (242 K) and finish at M_f (188 K). When we heat the sample upto the room temperature we found the Austenitic transformation starts at A_s (221 K) and finish at temperature A_f (264 K). To confirm that there is Austenitic to Martensitic transformation, we measured the magnetization of the sample in a constant field of 150 Oe in the temperature range 80 K to 400 K.

Through the XRD measurements we were able to characterize the structure of the alloy (See Figure 5). The XRD peaks were matched with the Full Prof Software and also with JCPD data base system. It has fcc austenite structure with the peaks at (110) and (211), at different positions and body centered cubic structure with peaks at different positions (111), (222) (see below). In addition there are some other peaks associated with gamma rich phases. These observations confirm the presence of austenitic phase and martensitic phase.

These observed XRD peaks clearly indicate that the as prepared alloy possess two phases beta (β) and gamma (γ) at room temperature. The Single phase (β) Ni-Fe-Al alloy shows very sharp martensitic transition, but has extremely low ductility at room temperature. The presence of the second phase (γ) with disordered fcc structure as a solid solution in NiFeAl system renders the β-phase ductile at room temperature and makes it useful for practical applications. (see [14])

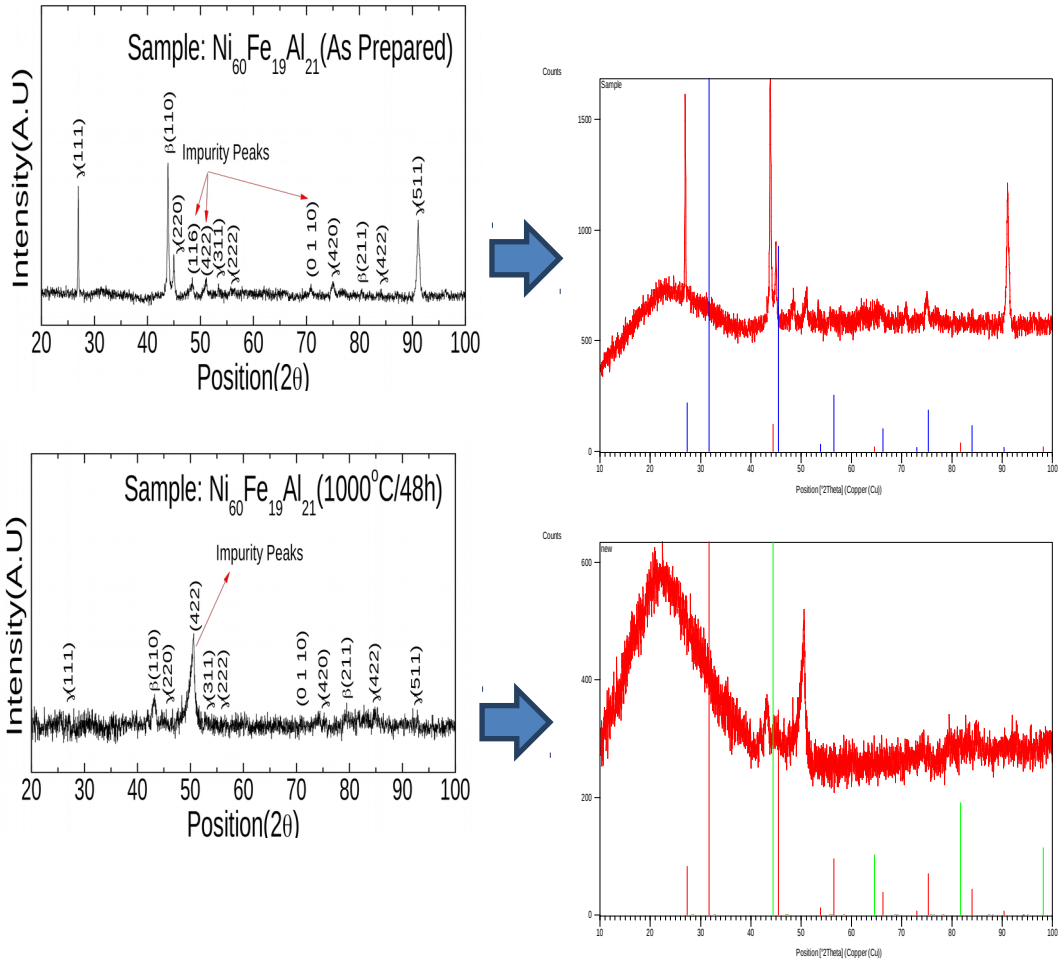

Figure 5- XRD observation for as prepared and annealed sample

4.2 FESEM Analysis

With the FESEM we are able to find the two phases in the NiFeAl alloy and this has been matched with the work done on FSMA NiFeAl alloy before. (see [15]) We have also confirmed this from our XRD analyses. In Figure 6a and 6b we show the FESEM images for as prepared sample and for the sample annealed at 1000^0 C. The Curie temperature of the unannealed sample is low, around 123K. Annealing the sample removes defects and is expected to bring the transition temperature range closer to the room temperature. As we anneal the sample at 1000 degree Celsius we expect the Curie temperature for the system to increase and come closer to the room temperature. (see reference [16]) We have also seen that annealing makes the structural transition from austenitic phase to martensitic phase closer to the range of room temperature around 300K. Therefore it is clear that annealing the sample is very important.

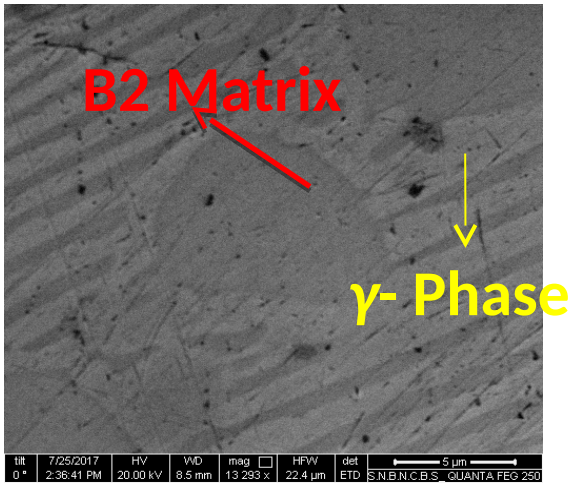

Fig 6a SEM of samples of as preparedprepared

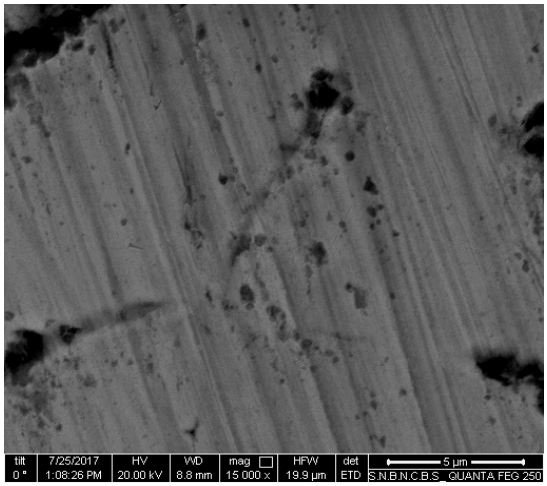

Fig 6b SEM of samples annealed at 1000oC/48h

5. CONCLUSION

In this paper we have focused on the synthesis and characterization study of the FSMA $Ni_{60}Fe_{19}Al_{21}$ alloy, which is an excellent alternate system for the commonly used FSMA, NiMnGa. In contrast to the low ductility of the Ga system, the Fe alloy has high ductility and it is not brittle. This makes the $Ni_{60}Fe_{19}Al_{21}$ alloy suitable as ferromagnetic shape memory alloy for application as actuators and sensors. In order to understand the full range of its properties one has to perform other measurements such as Differential Scanning Calorimetry and low temperature XRD. Further study will involve annealing the system at different temperatures and study how the FSM properties change with this in order to optimize the system for application.

6. REFERENCES

[1] P. K. Mukhopadhayay and S. N. Kaul: Appl. Phys. Lett. **92**, pp 101924 (2008).
[2] B. Rajini Kanth, P.K. Mukhopadhyay and S. N. Kaul: Adv. Materials Research **52** pp 129-133 (2008).
[3] R. K. Singh and R. Gopalan: Adv. Materials Research Vol. **52** pp 57-62 (2008).
[4] B. Rajini Kanth, N.V. Ramarao, A. K. Panda, R. Gopalan, A. Mitra, P. K. Mukhopadhayay: Jour. of Alloys and Compounds **491** 22 (2010).
[5] Madhusmita Baral and Aparna Chakrabarti: arXiv:1701.08282v2 (cond-mat. matrl-sci) 15/06/2017.
[6] V. A. Cherenko, E. Cesari, J. Pons, C.Segui, Jour. of Materials Res. **15** (2000) 1496.
[7] R. Kainuma, M. Ise, C-C. Jia, H. Ohtani and K. Ishida, Intermetallics **4** (1996) S151.
[8] K. Oikawa, T. Ota, F. Gejima, T. Ohmor, R. Kainuma, K. Ishida, Materials. Trans **42** (2001) 2472.
[9] K. Pushpanathan, R. Senthur Pandi, R. Chokkalingam, M. Mahendran, Advanced Material Research **52** pp 121-128 (2008).
[10] S. N. Kaul, B. Annie D'Santhosini, A. C. Abhayankar, Applied Phys. Letter. **89** (2006), 093119.
[11] Sarowar Hussain, P. K. Mukhopadhyay, B. Rajini Kanth, Springer 21/07/2017.
[12] Chengbao Jiang, https://www.researchgate.net/publication/223333223.
[13] F. X. hu, J. Shen, J. Wang, J. R. sun, B. G. Shen: https://doi.org/10.1016/j.jmmm.2009.03. 047
[14] B. Rajini Kanth, P.K.Mukhopadhyay**,** https://doi.org/10.1016/j.matpr.2016.11.056.
[15] H.Okumura, K.Uemura**,** https://doi.org/10.1016/j.intermet.2011.06.015.
[16] K. Oikawa, T. Omori, R. Kainuma, J. Magn. Magn. Mater, **272** p. 2043-2044 (2004).

Quantum First Passage Time Problem–A Bohmian Perspective

Siddhant Das*
Elite master program 'Theoretical and Mathematical Physics'
Arnold Sommerfeld Center, Ludwig-Maximilians-Universität München, Germany.

Abstract. The prediction of arrival time or first passage time statistics of a quantum particle is an open problem, which challenges the foundations of quantum theory. One of the most promising and insightful approaches to this problem stems from the de Broglie-Bohm pilot-wave theory (a.k.a Bohmian mechanics). Applying the fundamental postulates of this theory, we analyze a simplified first passage time experiment and derive the empirical passage time distribution $\Pi(\tau)$. Implications of our results are also discussed.
Keywords: arrival time operator, tunneling time, Bohmian mechanics, pilot-wave theory.

1. INTRODUCTION

In non-relativistic quantum mechanics, the probability of finding a particle in a small spatial volume d^3r around position $\boldsymbol{r}$ at a fixed time t is given by Born's rule $|\psi(\boldsymbol{r},t)|^2\mathrm{d}^3r$, where $\psi(\boldsymbol{r},t)$ is the wave function of the particle. However, a formula for the probability of finding the particle at a fixed point $\boldsymbol{r}$ between times t and $t+\mathrm{d}t$ is the matter of an ongoing debate. One might wonder, why is it so easy to speak about a position measurement at a fixed time, yet so hard to speak about a time measurement at a fixed position? For concreteness, consider the following experiment: a particle of mass m is prepared in the state[1]

$$\psi_0(\boldsymbol{r}) = \frac{e^{-\frac{1}{2}(r/a)^2}}{(\sqrt{\pi}\,a)^{3/2}} \tag{1}$$

at time $t=0$, where a is some fixed width of the wave function and $\boldsymbol{r} \equiv (r,\vartheta,\phi)$ are the standard spherical polar coordinates. A spherical detector placed at $r=d$ registers a click when the particle crosses $r=d$ and records the *first passage time* of the particle, denoted by τ. Let's assume that the experiment can be repeated several times, keeping ψ_0 unchanged in each run. Unsurprisingly, the detector click instants would vary from experiment to experiment, i.e., one would obtain a random sequence of passage times τ_1, τ_2, τ_3 ... What is the probability distribution of these passage times $\Pi(\tau)$ as a function of a and d?

The prediction of first passage times of a quantum particle has a long history [1, 2]. The very notion of arrival or passage time of a particle is not well posed within the orthodox (or Copenhagen) interpretation of quantum mechanics, since the particle is said to not have a well defined position at

*Siddhant.Das@physik.uni-muenchen.de
[1] State preparation is discussed in detail below.

a given instant of time. However, the problem of timing the motion of quantum particles surfaced long before any known interpretations of quantum mechanics came into being. As early as 1925, shortly after the invention of matrix mechanics, Wolfgang Pauli wrote to Niels Bohr:

"*In the new theory, all physically observable quantities still do not really occur. Absent, namely, are the time instants of transition processes, which are certainly in principle observable (as for example, are the instants of the emission of photoelectrons). It is now my firm conviction that a really satisfying physical theory must not only involve no unobservable quantities, but must also connect all observable quantities with each other. Also, I remain convinced that the concept of 'probability' should not occur in the fundamental laws of a satisfying physical theory.*" (§ 1.1 [1])

Pauli's early views on the problem of time in quantum mechanics greatly influenced the subsequent research on this subject. In particular, he showed that a self-adjoint time operator $\hat{T}$, canonically conjugate to the Hamiltonian $\hat{H}$, viz.

$$[\hat{H}, \hat{T}] = i\hbar \tag{2}$$

(just like position and momentum) implied that the spectrum of $\hat{H}$ would be *unbounded* from below, which in turn implied that matter couldn't be stable. This result raised doubts on the status of the 'time-energy uncertainty relation'

$$\Delta E \, \Delta T \geq \frac{\hbar}{2}. \tag{3}$$

Despite these impediments, many physicists have attempted to incorporate a respectable time observable by extending the basic framework of quantum theory (see [1, 2] for various attempts), although there is no general consensus among physicists on this subject.

The notion of arrival or first passage time is most naturally connected with that of particle trajectories, an idea not taken seriously, for example, in the Copenhagen interpretation of quantum mechanics. Therefore, it has long been realized that quantum theories comprising of actual particle trajectories, such as Bohmian Mechanics (a.k.a. de Broglie-Bohm pilot-wave theory, or the causal interpretation of quantum mechanics) provide a natural framework for addressing this problem.

In this theory, the idea of a particle is taken seriously, i.e., it is described as a point mass with a well defined trajectory $\boldsymbol{R}(t)$. The motion of the particle is choreographed by the wave function ψ, which satisfies the time dependent Schrödinger equation [3–5]. Guided by the wave function, the particle executes a highly non-Newtonian motion (hence the name pilot-wave), which underlies the wave-like properties seen in interference experiments. The theory is deterministic, hence the characteristic randomness of quantum mechanical experiments is understood as an artifact of one's ignorance of initial conditions. Bohmian mechanics is shown to be empirically equivalent to quantum mechanics in the sense that it makes the same predictions as orthodox quantum mechanics, whenever the latter is unambiguous [3, 4].

However, as indicated above, time measurements are problematic within the current formulation of quantum mechanics (also evidenced by recent attoclock experiments [6, 7]). While there are

a number of conflicting definitions of transit times, arrival times, etc., within orthodox quantum mechanics [1, 2], Bohmian mechanics privileges one, namely, the time taken by the Bohmian trajectory of the particle to strike a detector. Therefore, we ask: can the de-Broglie Bohm particle law of motion be made relevant to experiments? We try to answer this question in this paper, using the above experiment as a prototype. However, "we do not contest the correctness of quantum mechanics in the domain where it is *unambiguous*, testable and confirmed, but enquire whether that domain can be enlarged"(§ 5.5 [4]).

2. ELEMENTS OF BOHMIAN MECHANICS

In Bohmian mechanics a particle has a well defined position $\boldsymbol{R}(t)$ at time t, which is a vector in R^3. In the course of time, the particle moves on a deterministic (Bohmian) trajectory $\boldsymbol{R}$ with velocity vector $\dot{\boldsymbol{R}}$ specified by the guidance law

$$\dot{\boldsymbol{R}}(t) = \frac{\mathrm{d}}{\mathrm{d}t}\boldsymbol{R}(t) = \frac{\hbar}{m}\,\mathrm{Im}\left[\frac{\boldsymbol{\nabla}\psi}{\psi}\right](\boldsymbol{R}(t), t). \tag{4}$$

Here, $\psi(\boldsymbol{r}, t) \in \mathrm{C}$ is the wave function of the particle, which satisfies the Schrödinger equation

$$i\hbar\frac{\partial}{\partial t}\psi(\boldsymbol{r}, t) = -\frac{\hbar^2}{2m}\nabla^2\psi(\boldsymbol{r}, t) + V(\boldsymbol{r})\psi(\boldsymbol{r}, t) \tag{5}$$

with some initial condition $\psi(\boldsymbol{r}, 0) \equiv \psi_0(\boldsymbol{r})$. Equations (4) and (5) describe an isolated spin-0 particle of mass m and have analogues suitable for describing both multi-particle systems and particles with spin. The equations of motion in the latter cases are rather involved, and for simplicity will not be discussed here. The dynamical equations stated here are time reversal invariant, rotationally invariant, and the r.h.s. of (4) transforms as a velocity under Galilean boosts. These properties qualify Bohmian mechanics as a legitimate nonrelativistic theory. Applying Eq. (4) to any phenomena of interest, one obtains a very intuitive understanding of the actual dynamical processes at work, which are otherwise denigrated in the operational 'shut up and calculate' approaches (see [8–15] for many detailed examples). A satisfactory account of the theory can be found in [3–5].

As stated before, the probabilistic character of quantum mechanics arises in this theory as a consequence of ignorance of initial conditions, therefore the key insight for analyzing Bohmian mechanics lies within the foundations of statistical mechanics (especially in the ideas of Ludwig Boltzmann). This gives rise to the well known Born's rule [16], which states that the particle position at time t *is* distributed according to $|\psi(\boldsymbol{r}, t)|^2$, independent of any measurement prescription. In the next section we apply these basic principles to derive the empirical first passage time distribution $\Pi(\tau)$ for the experiment outlined above.

3. FORMULATION

The picture we have in mind is that the wave function $\psi(\boldsymbol{r}, t)$ evolves in time satisfying Eq. (5) with initial condition ψ_0, while the particle moves on a well defined Bohmian trajectory $\boldsymbol{R}(t)$ satisfying

(4), hence it's first passage time is unambiguously determined. One also needs to specify the initial position of the particle on the trajectory, viz. $\boldsymbol{R}(0) \equiv \boldsymbol{R}_0$ for solving Eq. (4). However, the particular $\boldsymbol{R}_0$ realized in an experiment is not known, hence the exact trajectory of the particle changes from experiment to experiment, and as a result the measured passage times appear random.

The first passage time of the particle is simply the first instant at which it's trajectory crosses $r = d$. More formally, we can write

$$\tau(\boldsymbol{R}_0) = \min\{t|\, R(t, \boldsymbol{R}_0) = d,\ \boldsymbol{R}_0 \in \mathrm{R}^3\}, \tag{6}$$

where $R(t, \boldsymbol{R}_0) = \|\boldsymbol{R}(t, \boldsymbol{R}_0)\|$ is the radial coordinate of the particle at time t. We have explicitly indicated that the first passage time on any trajectory depends on the initial position $\boldsymbol{R}_0$. However, definition (6) is incomplete, as it is not applicable to trajectories that *never* cross $r = d$. For such trajectories, we can set the passage time to ∞, since in these instances the detector would never click.

We return to a more detailed description of the experiment and the results. Introducing new dimensionless variables

$$\boldsymbol{r}' = \frac{\boldsymbol{r}}{a}, \quad d' = \frac{d}{a}, \quad \boldsymbol{R}' = \frac{\boldsymbol{R}}{a}, \quad \psi' = \frac{\psi}{a^{-3/2}}, \quad t' = \frac{\hbar}{ma^2}t, \tag{7}$$

we can rewrite the dynamical equations in a convenient nondimensionalized form, viz.,

$$\frac{\mathrm{d}}{\mathrm{d}t'}\boldsymbol{R}'(t') = \mathrm{Im}\left[\frac{\boldsymbol{\nabla}'\psi'}{\psi'}\right](\boldsymbol{R}'(t'), t'), \tag{8}$$

$$i\frac{\partial}{\partial t'}\psi'(\boldsymbol{r}', t') = -\frac{1}{2}\nabla'^2\psi'(\boldsymbol{r}', t'), \tag{9}$$

where $\boldsymbol{\nabla}'$ denotes the gradient w.r.t. the primed coordinates, and the external potential V has been set to zero. Henceforth, we will suppress the primes for brevity.

We begin by solving the time dependent Schrödinger equation (9) with initial condition $\psi_0(\boldsymbol{r}) = \pi^{-3/4}e^{-r^2/2}$. An easy way to accomplish this is by means of Fourier transforms. Employing standard Fourier transform conventions

$$\tilde{\psi}(\boldsymbol{k}, t) = \int_{\mathrm{R}^3} \mathrm{d}^3r\, e^{-i\,\boldsymbol{k}\cdot\boldsymbol{r}}\psi(\boldsymbol{r}, t), \tag{10a}$$

$$\psi(\boldsymbol{r}, t) = \int_{\mathrm{R}^3} \frac{\mathrm{d}^3k}{(2\pi)^3}\, e^{i\,\boldsymbol{k}\cdot\boldsymbol{r}}\tilde{\psi}(\boldsymbol{k}, t), \tag{10b}$$

we substitute Eq. (10b) into (9), obtaining

$$\frac{\partial}{\partial t}\tilde{\psi}(\boldsymbol{k}, t) = -i\frac{k^2}{2}\tilde{\psi}(\boldsymbol{k}, t) \Rightarrow \tilde{\psi}(\boldsymbol{k}, t) = A(\boldsymbol{k})e^{-i\frac{k^2}{2}t}. \tag{11}$$

Here, $A(\boldsymbol{k})$ is an arbitrary function of $\boldsymbol{k}$, which can be determined from the initial condition ψ_0. In particular,

$$A(\boldsymbol{k}) = \tilde{\psi}(\boldsymbol{k}, 0) = \int_{\mathrm{R}^3} \mathrm{d}^3r\, e^{-i\,\boldsymbol{k}\cdot\boldsymbol{r}}\psi_0(\boldsymbol{r}) = \pi^{-3/4}\int_{\mathrm{R}^3} \mathrm{d}^3r\, e^{-i\,\boldsymbol{k}\cdot\boldsymbol{r}-r^2/2} = (2\sqrt{\pi})^{3/2}e^{-k^2/2}, \tag{12}$$

where the integral is easily evaluated in Cartesian coordinates. Substituting (12) into (11), and the result into (10b), we obtain the time dependent wave function

$$\psi(\boldsymbol{r},t) = (2\sqrt{\pi})^{3/2}\int_{\mathrm{R}^3}\frac{\mathrm{d}^3k}{(2\pi)^3}\,e^{i\,\boldsymbol{k}\cdot\boldsymbol{r}-(1+it)\frac{k^2}{2}} = \frac{e^{-\frac{r^2}{2(1+it)}}}{(\sqrt{\pi}\,(1+it))^{3/2}}, \tag{13}$$

where the evaluation of the integral proceeds exactly as in (12). From (13) we see that the wave function propagates dispersively, i.e., it spreads isotropically in all directions with a width $\sigma(t) = \sqrt{1+t^2}$ that increases with time.[2]

Next, we look at the Bohmian trajectories, which are the integral curves of the Bohmian velocity field

$$\boldsymbol{v}_{\mathrm{Bohm}}(\boldsymbol{r},t) = \mathrm{Im}\left[\frac{\boldsymbol{\nabla}\psi}{\psi}\right](\boldsymbol{r},t) = \frac{t}{1+t^2}r\,\hat{\boldsymbol{r}}, \tag{14}$$

which in our case turns out to be a radial vector field. The particle position at time t is

$$\boldsymbol{R}(t) = R(t)\left[\cos\Theta(t)\sin\Phi(t)\,\hat{\boldsymbol{x}} + \sin\Theta(t)\sin\Phi(t)\,\hat{\boldsymbol{y}} + \cos\Phi(t)\,\hat{\boldsymbol{z}}\right], \tag{15}$$

the time derivative of which is

$$\dot{\boldsymbol{R}}(t) = \dot{R}(t)\,\hat{\boldsymbol{r}}(t) + R(t)\dot{\Theta}(t)\sin\Phi(t)\,\hat{\boldsymbol{\vartheta}}(t) + R(t)\dot{\Phi}(t)\,\hat{\boldsymbol{\phi}}(t), \tag{16}$$

where

$$\hat{\boldsymbol{r}}(t) = \cos\Theta(t)\sin\Phi(t)\,\hat{\boldsymbol{x}} + \sin\Theta(t)\sin\Phi(t)\,\hat{\boldsymbol{y}} + \cos\Phi(t)\,\hat{\boldsymbol{z}}, \tag{17a}$$

$$\hat{\boldsymbol{\vartheta}}(t) = -\sin\Theta(t)\,\hat{\boldsymbol{x}} + \cos\Theta(t)\,\hat{\boldsymbol{y}}, \tag{17b}$$

$$\hat{\boldsymbol{\phi}}(t) = \cos\Theta(t)\cos\Phi(t)\,\hat{\boldsymbol{x}} + \sin\Theta(t)\cos\Phi(t)\,\hat{\boldsymbol{y}} - \sin\Phi(t)\,\hat{\boldsymbol{z}}. \tag{17c}$$

The r.h.s of the guidance law (8) can be evaluated using Eq. (14), and comparison with the above derivative yields the component equations

$$\dot{R}(t) = \frac{t}{1+t^2}R(t), \quad R(t)\sin\Phi(t)\dot{\Theta}(t) = 0, \quad R(t)\dot{\Phi}(t) = 0. \tag{18}$$

If we let $R(t) = 0$, then all equations are trivially satisfied, however the initial condition $R(0) = R_0$ cannot be satisfied. For the same reason we cannot have $\sin\Phi(t) = 0$, hence the only remaining possibility is $\dot{\Phi}(t) = 0$ and $\dot{\Theta}(t) = 0$. These equations are readily solved:

$$\Theta(t) = \Theta_0, \quad \Phi(t) = \Phi_0, \tag{19}$$

which imply that the particle moves radially on a straight line. The differential equation for the radial coordinate is separable and admits a simple solution of the form

$$R(t) = R_0\sqrt{1+t^2}. \tag{20}$$

[2] By width we mean that of $|\psi| = \sqrt{\psi\,\psi^*}$.

Since $R(t) > 0$ for all t, the particle moves radially outwards with a *nonuniform* radial velocity (compare this with free Newtonian motion). However, as $t \to \infty$

$$R(t) = R_0 t \sqrt{1 + \frac{1}{t^2}} = R_0 t \left(1 + \frac{1}{2t^2} - \cdots\right) \sim R_0 t + \mathcal{O}(t^{-1}), \tag{21}$$

thus the velocity approaches R_0. This asymptotic radial velocity (restoring $\hbar$, m and a),

$$v_\infty = \frac{\hbar R_0}{ma^2}, \tag{22}$$

is a characteristic feature of free Bohmian motion. Note that particles starting far away from the centre of the wave packet acquire larger asymptotic velocities. In fact, all particles starting outside a sphere of radius a^2/λ_{c} acquire superluminal speeds as $t \to \infty$, where $\lambda_{\text{c}} = \hbar/mc$ is the (reduced) Compton wavelength. This shouldn't come as a surprise, since Eq. (8) and (9) (just like Newton's equations of motion) are only Galileian covariant, hence do not comply with the principles of special relativity.

Since the Bohmian trajectories propagate radially outward, any trajectory crosses $r = d$ only once, provided $R_0 < d$. The first passage time (or simply the passage time) τ can thus be determined by solving the equation $R(\tau) = d$, which yields (cf Eq. (6))

$$\tau(\boldsymbol{R}_0) = \begin{cases} \sqrt{(d/R_0)^2 - 1} & R_0 \leq d \\ \infty & R_0 > d \end{cases}. \tag{23}$$

We have set $\tau = \infty$ for all trajectories starting outside the detector, as they would not cross the detector in finite time. It must be remarked that Eq. (23) is exclusive to Bohmian mechanics with no known analogue in standard quantum mechanics. However, experience shows that in most situations of interest, the guidance law cannot be integrated analytically, hence an explicit formula connecting the passage time τ to the initial particle position $\boldsymbol{R}_0$, such as (23), cannot be found. Thus, one can typically at best approximate $\Pi(\tau)$ from a large number of Bohmian trajectories, which must be *computed numerically*.

We focus now on a derivation of the empirical passage time distribution $\Pi(\tau)$ for the case at hand. Recall that we are considering an ensemble of identically prepared experiments with $|\psi_0|^2$-distributed initial particle positions, hence the probability distribution of the passage time $\tau(\boldsymbol{R}_0)$ is given by

$$\Pi(\tau) = \int_{\mathrm{R}^3} \mathrm{d}^3 R_0 \, |\psi_0(\boldsymbol{R}_0)|^2 \, \delta(\tau(\boldsymbol{R}_0) - \tau), \tag{24}$$

where $\delta(x)$ is the Dirac delta function. Since $\tau(R_0) = \infty$ whenever $R_0 > d$, one has to cautiously deal with the object $\delta(\infty - \tau)$. This calls for a long mathematical digression, which is not absolutely necessary, for we may instead consider the statistics of a quantity related to τ, namely, its reciprocal

$$\nu(\boldsymbol{R}_0) = \tau^{-1}(\boldsymbol{R}_0) = \begin{cases} \frac{1}{\sqrt{(d/R_0)^2 - 1}} & R_0 \leq d \\ 0 & R_0 > d \end{cases}. \tag{25}$$

Note that the distribution of the first passage time τ, and that of it's reciprocal ν, are equivalent statistical characterizations, hence there is no loss of generality in analyzing the latter. We do so, of course, because it is more amenable to mathematical analysis. Analogous to Eq. (24), the distribution of the reciprocal passage time $\nu(\boldsymbol{R}_0)$ can be written as

$$\Lambda(\nu) = \int_{\mathrm{R}^3} \mathrm{d}^3 R_0 \, |\psi_0(\boldsymbol{R}_0)|^2 \, \delta(\nu(\boldsymbol{R}_0) - \nu) = 4\pi \int_0^\infty \mathrm{d}R_0 \, R_0^2 \, |\psi_0(\boldsymbol{R}_0)|^2 \, \delta(\nu(\boldsymbol{R}_0) - \nu), \tag{26}$$

where the factor of 4π results from integrating over the angular coordinates of $\boldsymbol{R}_0$. Substituting $|\psi_0(\boldsymbol{R}_0)|^2 = \pi^{-3/2} e^{-R_0^2}$, and Eq. (25), we arrive at

$$\Lambda(\nu) = \frac{4}{\sqrt{\pi}} \int_0^d \mathrm{d}R_0 \, R_0^2 \, e^{-R_0^2} \, \delta\left(\frac{1}{\sqrt{(d/R_0)^2 - 1}} - \nu \right) + \frac{4}{\sqrt{\pi}} \, \delta(\nu) \int_d^\infty \mathrm{d}R_0 \, R_0^2 \, e^{-R_0^2}. \tag{27}$$

The second integral multiplying $\delta(\nu)$, which we denote by $\alpha(d)$, can be evaluated relatively easily:

$$\begin{aligned} \alpha(d) = \frac{4}{\sqrt{\pi}} \int_d^\infty \mathrm{d}R_0 \, R_0^2 \, e^{-R_0^2} &= -\frac{2}{\sqrt{\pi}} \int_d^\infty \mathrm{d}\left(e^{-R_0^2}\right) R_0 \\ &= -\frac{2}{\sqrt{\pi}} \, R_0 \, e^{-R_0^2} \Big|_d^\infty + \frac{2}{\sqrt{\pi}} \int_d^\infty \mathrm{d}R_0 \, e^{-R_0^2} \qquad \text{(integrating by parts)} \\ &= \frac{2d}{\sqrt{\pi}} e^{-d^2} + \mathrm{erfc}(d), \end{aligned} \tag{28}$$

where $\mathrm{erfc}(x)$ is the complementary error function (see Eq. (2.1.6) of [17]). In retrospect, we see that α is simply the probability of finding the particle outside the detector at $t = 0$.[3] Equation (27) can thus be written as

$$\Lambda(\nu) = \frac{4}{\sqrt{\pi}} \int_0^d \mathrm{d}R_0 \, R_0^2 \, e^{-R_0^2} \, \delta\left(\frac{1}{\sqrt{(d/R_0)^2 - 1}} - \nu \right) + \alpha(d) \, \delta(\nu). \tag{29}$$

In order to evaluate the remaining integral in (29), we recall a useful identity of the Dirac delta function:

$$\delta(f(x)) = \sum_n \frac{\delta(x - x_n)}{|f'(x_n)|}, \tag{30}$$

where x_n is a zero of the function f (an x for which $f(x) = 0$), f' denotes its derivative, and the sum runs over all (real) zeros of f. Choosing

$$f(R_0) = \frac{1}{\sqrt{(d/R_0)^2 - 1}} - \nu, \tag{31}$$

[3] In real experiments the initial wave function is expected to vanish outside the detector, hence $\alpha = 0$. Naturally, this would spare us the technical problems posed by the initial conditions lying outside the detector. However, the time evolution of such compactly supported wave packets gets quite messy, which is avoided here for simplicity.

we obtain two zeros, viz.,

$$R_0^{\pm} = \pm \frac{\nu}{\sqrt{1+\nu^2}} d, \tag{32}$$

and evaluating the derivatives of f at $R_0^{\pm}$, we find (applying (30)):

$$\delta\left(\frac{1}{\sqrt{(d/R_0)^2-1}} - \nu\right) = \frac{|R_0|^3}{d^2\nu^3}\Big(\delta(R_0 - R_0^+) + \delta(R_0 - R_0^-)\Big). \tag{33}$$

Since $R_0^- < 0$, only the first delta function term fires in the region of integration (cf Eq. (29)), the integral is thus easily evaluated. After a few rounds of simplification, we obtain

$$\Lambda(\nu) = \frac{4d^3}{\sqrt{\pi}} \frac{\nu^2}{(1+\nu^2)^{5/2}} \exp\left(-\frac{\nu^2}{1+\nu^2} d^2\right) + \alpha(d)\,\delta(\nu). \tag{34}$$

We shall refer to the first (second) summand above as the *continuous* (*singular*) part of $\Lambda(\nu)$. The continuous part has been graphed in Fig. 1 for different values of d.

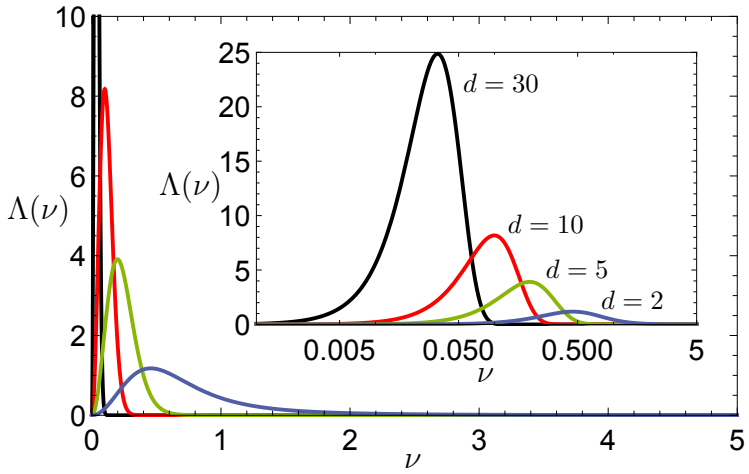

Figure 1. Graphs of the continuous part of $\Lambda(\nu)$ vs. ν for different values of d. Inset: log-linear plot of the same curves.

The reciprocal passage time distribution $\Lambda(\nu)$ has many interesting properties. First, we see from Fig. 1 that the continuous part of the distribution becomes sharply peaked as d becomes large, which implies that the first passage time distribution $\Pi(\tau)$ broadens with increasing d. In fact, as $d \to \infty$, $\alpha \to 0$ (see Fig. 2 inset), hence the singular part of $\Lambda(\nu)$ vanishes, while the continuous part tends to $\delta(\nu)$. This is reasonable, since the particle takes an infinite amount of time to cross a detector placed at infinity, hence the reciprocal passage time $\nu = 0$ for all Bohmian trajectories.
On the other hand, as $d \to 0$, i.e. as the detector shrinks to a point, all initial positions of the particle fall outside the detector volume, hence it never crosses the detector, consequently $\tau = \infty$ (or $\nu = 0$) for all Bohmian trajectories and $\Lambda(\nu) \to \delta(\nu)$. The same conclusion follows from formula (34),

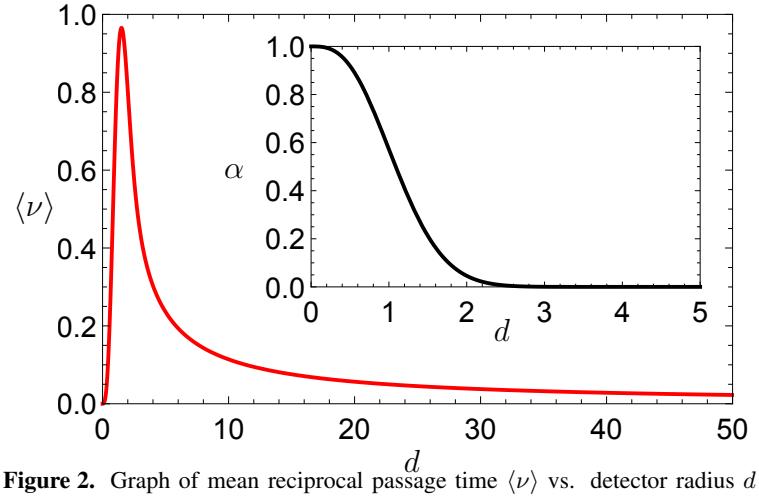

Figure 2. Graph of mean reciprocal passage time $\langle\nu\rangle$ vs. detector radius d (cf Eq. (36)). Inset: Graph of α vs. detector radius d (cf Eq. (28)).

since the continuous part now vanishes as $d \to 0$, while $\alpha \to 1$. Remarkably, in both limits $\Lambda(\nu)$ approaches a delta function, although for very different physical reasons.

Now, keeping d fixed, we find that the continuous part of $\Lambda(\nu)$ grows as a power law $\sim \nu^2$ as ν approaches zero, and falls off as an inverse cube:

$$\Lambda(\nu) \sim \frac{4d^3}{\sqrt{\pi}}\,\frac{e^{-d^2}}{\nu^3} + \mathcal{O}\big(\nu^{-4}\big) \tag{35}$$

as $\nu \to \infty$. This implies that the mean reciprocal passage time $\langle\nu\rangle$ exists, i.e. it is finite, while its variance (or any higher cumulant) does not. Such distributions are said to be 'heavy tailed'. We can also calculate $\langle\nu\rangle$ explicitly:

$$\begin{aligned}
\langle\nu\rangle &= \int_0^\infty \mathrm{d}\nu\, \nu\, \Lambda(\nu) = \frac{4d^3}{\sqrt{\pi}} \int_0^\infty \mathrm{d}\nu\, \frac{\nu^3}{(1+\nu^2)^{5/2}}\, \exp\!\left(-\frac{\nu^2}{1+\nu^2}\, d^2\right) \,+\, \alpha(d) \int_0^\infty \mathrm{d}\nu\, \nu\, \delta(\nu) \\
&= \frac{2\,d^3}{\sqrt{\pi}} e^{-d^2} \int_0^1 \mathrm{d}x\, x^{-1/2}(1-x)\, e^{d^2 x} \,+\, 0 \qquad \text{(substituting } x = (1+\nu^2)^{-1}\text{)} \\
&= \frac{2\,d^3}{\sqrt{\pi}} e^{-d^2} \times \frac{\Gamma(2)\Gamma\left(\frac{1}{2}\right)}{\Gamma\left(\frac{5}{2}\right)}\, {}_1F_1\!\left(\frac{1}{2}; \frac{5}{2}; d^2\right) \qquad \text{(see Eq. (9.11.1) of [17])} \\
&= \frac{8\,d^3}{3\sqrt{\pi}}\, {}_1F_1\!\left(\frac{1}{2}; \frac{5}{2}; d^2\right) e^{-d^2},
\end{aligned} \tag{36}$$

where ${}_1F_1(a;b;z)$ is the confluent hypergeometric function of the first kind.[4] We graph Eq. (36) in Fig. 2. Note that $\langle\nu\rangle$ vanishes as $d \to 0$, and as $d \to \infty$, which is consistent with our earlier observations.

[4] In Ref. [17] ${}_1F_1(a;b;z)$ is denoted by $\Phi(a,b;z)$.

4. CONCLUSION

In the framework of Bohmian theory, we have derived the empirical first passage time distribution of a free particle, which has a satisfactory physical interpretation. Generally, these distributions depend strongly on the initial wave function of the particle. However, some of the features discussed here, for instance the behavior of $\Lambda(\nu)$ as $d \to \infty$ is rather universal. Therefore, in order to observe our results in real experiments one must prepare the initial wave function as accurately as possible.

A simple preparation procedure for realizing a desired ψ_0 was outlined by W. E. Lamb in [18]. The basic idea involves 1.) setting up a potential well $V(\boldsymbol{r})$ in some region of space, with ψ_0 being the ground state wave function of V, 2.) directing the particle from a source to this region, and 3.) waiting for radiation damping (or spontaneous emission) to bring the particle to the ground state. In the final step 4.), the potential V is switched off *suddenly*, allowing the particle to propagate freely in space. If the switching off is sufficiently fast, ψ_0 is left undisturbed. For preparing the initial wave function (1) we can choose $V(\boldsymbol{r}) = \frac{1}{2}m\omega^2 r^2$–a three dimensional isotropic harmonic potential–whose ground state wave function is a well known Gaussian (see § 13.2 of [19]), which exactly equals (1) with $a = \sqrt{\frac{\hbar}{m\omega}}$. Therefore, appropriately tuning the trapping frequency ω, one can fix the width a to any desired value.

A final remark concerning the implications of our results is in order. Formula (24) (or (26)) generally yields results different from other approaches, hence the possibility of experimentally distinguishing various proposals exists. With state of the art experimental technology, such as attosecond spectroscopy, our proposals might be checked in future experiments. "*Although empirical confirmation of these predictions would not prove the 'reality' of the particle trajectory, it would provide strong circumstantial evidence in its favour, being a test of the particle law of motion*" [4].

ACKNOWLEDGEMENTS

I would like to thank Dr. J. M. Wilkes for critically reviewing this manuscript. The presentation of the paper improved greatly from Dr. Mike's suggestions. Dr. S. D. Mahanti inspired me to transcribe my seminar talk in the form of a paper for the Student Journal of Physics of IAPT. I thank him for his kind encouragement and continued support throughout the process. This paper is dedicated to Dr. Prof. Detlef Dürr for introducing me to this fascinating subject and for being a benevolent research partner ever since.

References

[1] J. G. Muga, R. Sala Mayato, and Í. L. Egusquiza, editors. *Time in Quantum Mechanics*, volume 1 of *Lecture Notes in Physics 734*. Springer, Berlin, Heidelberg, second edition, 2008.

[2] J. G. Muga and C. R. Leavens. Arrival time in quantum mechanics. *Physics Reports*, 338(4):353–438, 2000.

[3] D. Dürr and S. Teufel. *Bohmian Mechanics-The Physics and Mathematics of Quantum Theory*. Springer, Heidelberg, 2009.

[4] P. R. Holland. *The Quantum Theory of Motion*. Cambridge University Press, NY, 1993.

[5] D. Bohm and B. J. Hiley. *The Undivided Universe: An Ontological Interpretation of Quantum Theory*. Routledge, London and New York, 1993.

[6] A. S. Landsman, M. Weger, J. Maurer, R. Boge, A. Ludwig, S. Heuser, C. Cirelli, L. Gallmann, and U. Keller. Ultrafast resolution of tunneling delay time. *Optica*, 1:343–349, 2014.

[7] T. Zimmermann, S. Mishra, B. R. Doran, D. F. Gordon, and A. S. Landsman. Tunneling time and weak measurement in strong field ionization. *Physical Review Letters*, 116:233603, 2016.

[8] T. Norsen. The pilot-wave perspective on quantum scattering and tunneling. *American Journal of Physics*, 81(4):258–266, 2013.

[9] A. Cesa, J. Martin, and W. Struyve. Chaotic Bohmian trajectories for stationary states. *Journal of Physics A: Mathematical and Theoretical*, 49(39):395301, 2016.

[10] R. Dubertrand, S. Jeong-Bo, and W. Struyve. Bohmian trajectories for the half-line barrier. *The Journal of Physics A: Mathematical and Theoretical*, 51(8):085302, 2018.

[11] C. Dewdney, P. R. Holland, C. Kyprianidis, and J. P. Vigier. Spin and non-locality in quantum mechanics. *Nature*, 336:536–544, 1988.

[12] C. Colijn and E. R. Varscay. Spin-dependent Bohm trajectories for hydrogen eigenstates. *Physics Letters A*, 300:334–340, 2002.

[13] C. Colijn and E. R. Varscay. Spin-dependent Bohm trajectories for Pauli and Dirac eigenstates of hydrogen. *Foundations of Physics Letters*, 16:303–323, 2003.

[14] C. Colijn and E. R. Varscay. Spin-dependent Bohm trajectories associated with an electronic transition in hydrogen. *Journal of Physics A: Mathematical and General*, 36:4689, 2003.

[15] J. A. Timko and E. R. Vrscay. Spin-dependent Bohmian electronic trajectories for helium. *Foundations of Physics*, 39:1055–1071, 2009.

[16] D. Dürr, S. Goldstein, and N. Zanghì. Quantum equilibrium and the origin of absolute uncertainty. *Journal of Statistical Physics*, 67:843–907, 1992.

[17] N. N. Lebedev and R. A. Silverman. *Special Functions and Their Applications*. Prentice Hall, NJ, 1965.

[18] Willis E. Lamb. An operational interpretation of nonrelativistic quantum mechanics. *Physics Today*, 22(4), 1969.

[19] S. Brandt and D. H. Dahmen. *The Picture Book of Quantum Mechanics*. Springer-Verlag, NY, third edition, 2001.

STUDENT JOURNAL OF PHYSICS

Volume 6 **Number 4** **Oct - Dec 2017**

CONTENTS

ARTICLES